

OPTICAL AND ULTRAVIOLET SPECTROSCOPY OF SN 1995N:

EVIDENCE FOR STRONG CIRCUMSTELLAR INTERACTION¹

Claes Fransson², Roger A. Chevalier³, Alexei V. Filippenko⁴, Bruno Leibundgut⁵, Aaron J. Barth^{6,7}, Robert A. Fesen⁸, Robert P. Kirshner⁶, Douglas C. Leonard^{4,9}, Weidong Li⁴, Peter Lundqvist², Jesper Sollerman⁵, and Schuyler D. Van Dyk¹⁰

ABSTRACT

Optical and ultraviolet observations of the Type II_n supernova 1995N at epochs between 321 and 1799 days after the explosion show three distinct velocity components. The narrow lines come from circumstellar gas and show both low and high ionization. This component has a low filling factor, and is photoionized by X-rays from the shock. The intermediate component, which is dominated by newly processed oxygen, originates in a shell with velocity of 2500–5000 km s⁻¹, and most likely comes from the ejecta. The hydrogen- and helium-dominated gas has a low ionization, a high density, and velocities that

¹Based in part on observations obtained with the *Hubble Space Telescope*, which is operated by AURA, Inc., under NASA contract NAS 5-26555; in part on observations collected at the European Southern Observatory, Paranal, Chile; in part on data from the Lick Observatory, California; and in part on observations from the Keck Observatory, Hawaii.

²Stockholm Observatory, SE-133 36 Saltsjöbaden, Sweden.

³Department of Astronomy, University of Virginia, P.O. Box 3818, Charlottesville, VA 22903.

⁴Department of Astronomy, University of California, Berkeley, CA 94720-3411.

⁵European Southern Observatory, Karl-Schwarzschild-Strasse 2, D-85748 Garching, Germany.

⁶Harvard-Smithsonian Center for Astrophysics, 60 Garden St., Cambridge, MA 02138.

⁷Present address: Department of Astronomy, 105-24 Caltech, Pasadena, CA 91125.

⁸6127 Wilder Laboratory, Physics & Astronomy Department, Dartmouth College, Hanover, NH 03755.

⁹Present address: Five College Astronomy Department, University of Massachusetts, Amherst, MA 01003-9305.

¹⁰IPAC, 100-22 Caltech, Pasadena, CA 91125.

extend out to $\gtrsim 10,000 \text{ km s}^{-1}$. Strong signatures of Ly α -pumped fluorescence lines of Fe II are seen in the near-infrared and ultraviolet. The He/H ratio, ~ 0.3 by number, and the nitrogen overabundance provide strong evidence for CNO burning products. The fluxes of the broad hydrogen and helium lines decrease considerably faster than the oxygen lines. The H α line profile shows strong evolution, with the red wing decreasing faster than the blue. Possible scenarios, involving either a clumpy circumstellar medium, or an aspherical distribution of the surrounding gas, are discussed based on the line profiles and physical conditions. Finally, we propose that Type IIn supernovae have their origin in red supergiants in a superwind phase.

Subject headings: stars: circumstellar matter — stars: mass loss — supernovae: individual: SN 1995N

1. INTRODUCTION

SN 1995N in MCG–02-38-017 (also known as Arp 261) was discovered by Pollas (1995) on 5 May 1995 (UT dates are used throughout this paper). Its approximate distance is 24 Mpc, based on $H_0 = 75 \text{ km s}^{-1} \text{ Mpc}^{-1}$ and the measured recession velocity of the host galaxy (1834 km s^{-1} ; Theureau et al. 1998). Optical spectra of the object obtained by Benetti, Bouchet, & Schwarz (1995) and by Garnavich & Challis (1995) showed it to be a peculiar Type II supernova, with H α emission (full-width at half-maximum intensity [FWHM] $\approx 1500 \text{ km s}^{-1}$) and narrow lines of He I, He II, [N II], [O I], [O III], [Ne III], [Ca V], Fe II, [Fe II], [Fe III], [Fe VII], and [Fe X]. The intensity ratios of the narrow oxygen lines suggest a high electron density, $> 10^6 \text{ cm}^{-3}$ (Garnavich & Challis 1995). Benetti et al. (1995) estimated it to be at least 10 months old, so we will assume an explosion date of 4 July 1994, befitting for a supernova (in the opinion of the U.S. coauthors of this paper). Radio emission from the supernova was discovered at 3.6 cm on 16 June 1995 (Van Dyk et al. 1996). X-ray emission was discovered with *ROSAT* on 23 July 1996, and the source was subsequently observed with *ASCA* on 20 January 1998 (Fox et al. 2000). The unabsorbed X-ray luminosity was $1 \times 10^{41} \text{ erg s}^{-1}$ in the 0.1–10 keV band.

The narrow emission lines observed from SN 1995N place it in the Type IIn category (Schlegel 1990; Filippenko 1991a,b, 1997), which often show a slow optical decline compared to other Type II supernovae (SNe II). Baird et al. (1998) have noted the slow evolution of SN 1995N. The high X-ray and radio luminosities of SN 1995N place it in a subset of SNe IIn whose other well-studied members are SN 1986J (Rupen et al. 1987; Weiler, Panagia, & Sramek 1990; Leibundgut et al. 1991; Houck et al. 1998), SN 1988Z (Stathakis & Sadler

1991; Filippenko 1991a,b; Turatto et al. 1993; Van Dyk et al. 1993; Fabian & Terlevich 1996; Aretxaga et al. 1999), SN 1978K (Ryder et al. 1993; Chugai, Danziger, & Della Valle 1995; Schlegel, Petre, & Colbert 1996), and SN 1998S (Leonard et al. 2000, Gerardy et al. 2000; Fassia et al. 2001). All of them have X-ray luminosities $\gtrsim 10^{40}$ erg s $^{-1}$, which are at least an order of magnitude higher than the X-ray luminosities of other SNe II. These are also among the most luminous radio SNe, although SN 1979C does rival them in luminosity, as does SN 1998bw, a very different kind of object and at a much earlier epoch (e.g., Galama et al. 1998; Kulkarni et al. 1998).

The early optical observations of SN 1988Z (Stathakis & Sadler 1991) showed velocities up to $\sim 20,000$ km s $^{-1}$, and very long baseline interferometry (VLBI) radio observations of SN 1986J (Bartel, Shapiro, & Rupen 1989; Bartel et al. 1991) implied expansion velocities of $\sim 15,000$ km s $^{-1}$. At the same time, these SNe showed H α emission lines with FWHM $\approx 500 - 2000$ km s $^{-1}$, and at least SN 1988Z exhibited very narrow emission lines whose intensity ratios indicate high gas densities. This combination suggests that the rapidly moving supernova material is running into dense circumstellar clumps and is driving slower shock fronts into them (Chugai 1993; Chugai & Danziger 1994; Chugai et al. 1995). In addition, the combination of high velocities with strong circumstellar interaction requires that the supernova have considerable high-velocity gas in order not to be rapidly decelerated. For SN 1988Z, Chugai & Danziger (1994) estimate that the total mass in supernova ejecta is only $\sim 0.5 M_{\odot}$ if the explosion energy is the standard 10^{51} ergs.

In order to more fully understand the nature of this peculiar subset of SNe II n , we have undertaken a detailed spectroscopic study of SN 1995N, one of the most important and thoroughly studied examples. We present the ground-based and *Hubble Space Telescope* (*HST*) observations in § 2. In § 3, we discuss the three main kinematic components visible in the emission-line profiles. Synthetic spectra are presented in § 4, and the temporal evolution of features is examined in § 5. We discuss the results and their implications in § 6, and we summarize our conclusions in § 7.

2. OBSERVATIONS

Figure 1 shows a 3-minute *R*-band image of MCG–02-38-107 and SN 1995N taken with the FORS1 instrument on the ESO Very Large Telescope (VLT) on 11 May 1999 (UT dates are used throughout this paper). Figure 2 is an *HST* WFPC2 *I*-band (F814W) image of SN 1995N obtained on 22 July 2000; the supernova is easily visible at ~ 20.5 mag. These two images demonstrate that the supernova occurred in a region relatively free of background emission and dust.

The main observations of SN 1995N presented in this paper consist of ground-based optical spectra obtained on nine epochs and ultraviolet (UV) *HST* spectra on one epoch. The log of the observations is given in Table 1, where the wavelength ranges, UT dates, and approximate epoch since explosion are summarized. The assumed explosion date of 4 July 1994 is uncertain, but this does not appreciably affect our results because our data were taken long after the explosion; the spectra cover epochs of 321–1799 days. Standard procedures were followed for the spectral extractions and reductions, which included sky subtraction, wavelength and flux calibration, and removal of telluric absorption (e.g., Matheson et al. 2000).

The ground-based observations fall in two main groups: within ~ 2 years after discovery, and ~ 4 years after discovery. The former were obtained primarily with the Kast spectrograph (Miller & Stone 1993; 2" slit) on the 3-m Shane reflector at Lick Observatory, but the Low Resolution Imaging Spectrometer (LRIS; Oke et al. 1995; 1" slit) on the Keck-I telescope was used to acquire an excellent spectrum (day 1007) nearly contemporaneously with one of the Lick spectra (day 1012). All of the Lick and Keck spectra (except day 1012) are shown in Figure 3. One can see that the spectrum evolved slowly during the time interval shown. In this paper, we present a detailed analysis of only two of these spectra (days 716 and 1007, which are among the two best ones).

The very late-time (~ 4 years) ground-based spectra were taken through a 1" slit with FORS1 on the VLT at ESO. The day 1769 spectrum was obtained with gratings 300V and 300I, giving a resolution of ~ 13 Å. For the day 1799 spectrum the 600B, 600R, and 600I grisms were used, giving a higher resolution of ~ 5 Å. The day 1769 observing was done in good conditions, while the data from day 1799 were taken through clouds. The latter spectrum has higher signal-to-noise ratio (S/N) than the former, however, so emission-line measurements are reported for it (scaled to the flux level of the day 1769 spectrum).

The *HST* spectra on day 943 were obtained with the Faint Object Spectrograph (FOS) with the G400H, G270H, and G160L gratings. Total exposures times were 2860, 4770, and 2110 s, and the resolution was 3.0, 2.1, and 6.9 Å per diode, respectively. The spectra were calibrated by the FOS pipeline at the Space Telescope Science Institute.

All spectra, except the VLT and *HST* spectra, were calibrated to the *V*-band and *R*-band photometry of Baird et al. (1998). The Keck spectrum (day 1007) has the highest S/N , and in Figure 4 we show it together with the *HST* spectra (day 943). The Keck and *HST* spectra were taken at different epochs, but from the day 1037 Lick spectrum we find a smooth evolution, and we normalize the flux level of the overlapping region between the *HST* G400H spectrum and the Keck spectrum to that of the Keck epoch.

The Dirbe/IRAS maps (Schlegel, Finkbeiner, & Davis 1998) give $E_{B-V} = 0.11$ mag for the Galactic reddening of SN 1995N. In addition, there could be internal reddening from both the host galaxy and the circumstellar environment. The host galaxy is a blue compact galaxy, a class which is generally dust-poor, although H II regions can show substantial reddening (Kong & Cheng 1999). The fact that the supernova is located in the outskirts of the galaxy (Figures 1, 2) also makes it natural to expect a relatively low extinction. From the relative strengths of the higher members of the H I and He I recombination series, there is no indication of strong reddening (§ 4.1). The normal intensity ratio of UV [O III] lines relative to the optical also indicates this. In the following, we use $E_{B-V} = 0.11$ mag for the total reddening.

3. KINEMATIC COMPONENTS

Figure 4 shows that there are lines spanning a large range of velocities, and we can distinguish at least three kinematic components in the supernova. The narrow, unresolved lines are clearly distinct, while the other two components are less obvious and are shown in the Mg II $\lambda\lambda 2796, 2803$, [O III] $\lambda\lambda 4959, 5007$, and H α lines at 943–1007 days on the same velocity scale in Figure 5. The H α and [O III] profiles are from the Keck day 1007 spectrum and the Mg II profile from the *HST* spectrum. The H α and [O III] lines have quite different profiles, with the former having a fairly peaked profile, but with weak wings reaching very high velocity, $\sim 10,000$ km s $^{-1}$, while the latter has a more boxy profile reaching a velocity of ~ 5000 km s $^{-1}$. Another strong indication of two separate high-velocity components is the different temporal evolution of the [O I], [O II], and [O III] lines compared to the others (§ 5). Here we discuss these three components individually.

3.1. Narrow Lines

The narrowest lines in the spectra are unresolved, implying FWHM $\lesssim 500$ km s $^{-1}$. They are listed in Table 2, where it can be seen that the emission is dominated by ions with moderately high ionization. Some of the lines provide useful diagnostics for the emitting region, and we begin by considering them.

[O III]. The [O III] $\lambda\lambda 4959, 5007$ lines are by far the strongest narrow lines and, together with [O III] $\lambda 4363$, provide a useful constraint on the electron temperature T and the electron density n_e . The relatively low ratio of $I(\lambda 4959 + \lambda 5007)/I(\lambda 4363) = 5.4$ implies that collisional deexcitation of the 1D_2 level is important, so that the ratio depends on

density as well as temperature (e.g., Filippenko & Halpern 1984; Osterbrock 1989). The densities corresponding to various assumed temperatures are in the range $7.3 \times 10^5 < n_e < 7.5 \times 10^7 \text{ cm}^{-3}$ for $0.8 < T_4 < 4$ (or $7.3 \times 10^5 < n_e < 2.0 \times 10^6 \text{ cm}^{-3}$ for $0.8 < T_4 < 2$), where $T_4 = T/(10^4 \text{ K})$. On day 1799 the VLT spectrum shows a similar value, $I(\lambda 4959 + \lambda 5007)/I(\lambda 4363) = 6.5$, which gives $7 \times 10^5 < n_e < 4 \times 10^6 \text{ cm}^{-3}$ for $1 < T_4 < 2$.

O III Bowen lines. In the near-UV spectral region, several Bowen fluorescence lines are seen, most notably O III $\lambda\lambda 3047, 3133, 3340, 3444$. We measure $I(\lambda 3047)/I(\lambda 3132) \approx 0.30$ and $I(\lambda 3444)/I(\lambda 3132) \approx 0.25$. Based on the Bowen process, Kallman & McCray (1980) give ratios of 0.18 and 0.28 for these lines, respectively. Considering that the uncertainties in the fluxes of both lines are at least a factor of two, the agreement is satisfying. The $\lambda 3340$ line is severely blended with [Ne III] $\lambda 3342$ and [Ne V] $\lambda 3345$, and no reliable flux estimate can be obtained.

The ratio $I(\text{O III } \lambda 3132)/I(\text{He II } \lambda 4686)$ can be used to estimate the Bowen yield for He II $\lambda 304$. Equation (25) in Kallman & McCray (1980), together with $I(\lambda 3444)/I(\lambda 3132) = 0.28$, gives a Bowen yield of $y_B = 0.28 \times I(\text{O III } \lambda 3132)/I(\text{He II } \lambda 4686)$. Correcting for reddening, we find $I(\text{O III } \lambda 3132)/I(\text{He II } \lambda 4686) = 1.05$, and therefore $y_B \approx 0.3$ for SN 1995N at day 1007. As a comparison, Schachter, Filippenko, & Kahn (1990) find a mean $y_B \approx 0.24$ for a sample of Seyfert nuclei, while Kallmann & McCray find that planetary nebulae have $y_B \approx 0.37$. The dispersion in both values is considerable.

[O II]. The spectra show that [O II] $\lambda\lambda 3726, 3729$ are not detected, but that [O II] $\lambda\lambda 7320, 7330$ are weakly present with narrow components. The fact that $I(\lambda 3726 + \lambda 3729)/I(\lambda 7320 + \lambda 7330) < 1$ implies that $n_e > 3 \times 10^4 \text{ cm}^{-3}$, provided that $T < 30,000 \text{ K}$.

[N II]. The auroral [N II] $\lambda 5755$ line is present, but the nebular lines are superposed on the very strong H α emission and it is not possible to obtain strong limits on them. We estimate $I(\lambda 6548 + \lambda 6583)/I(\lambda 5755) < 12$, which implies that $n_e > 6 \times 10^4 \text{ cm}^{-3}$ for $T \approx 20,000 \text{ K}$ (Osterbrock 1989).

[Fe VII]. The observed lines of [Fe VII] are $\lambda\lambda 3586, 3759, 5159, 5276, 5721, 6087$. As discussed by Nussbaumer & Storey (1982) and Keenan & Norrington (1987, 1991), several of the [Fe VII] lines provide diagnostic information on the emitting region. There is temperature sensitivity of the lines, and collisional deexcitation causes transitions from the low-density limits to the high-density limits in the range $n_e \approx 10^6 - 10^8 \text{ cm}^{-3}$.

The observed, reddening-corrected ratio $I(\lambda 3759)/I(\lambda 6087) \approx 0.83$ in the Keck spectrum (day 1007), and ~ 1.1 in the 12 June 1999 VLT spectrum (day 1799). From Figure 2 of Keenan & Norrington (1987), this sets a limit $T > 17,000 \text{ K}$ for any density on day 1007, and $T > 22,000 \text{ K}$ for day 1799.

In the day 1799 spectrum, with the highest resolution, there are three distinct peaks at the positions of [Fe VI] $\lambda 5146$, [Fe VII] $\lambda 5159$, and [Fe VI] $\lambda 5176$. Because of blending of these lines, it is difficult to obtain accurate fluxes, and depending on where we estimate the base of the line we get a ratio in the range $0.20 \lesssim I(\lambda 5159)/I(\lambda 6087) \lesssim 0.73$ and $0.25 \lesssim I(\lambda 5159)/I(\lambda 6087) \lesssim 1.1$ on days 1007 and 1799, respectively. From Figure 1 of Keenan & Norrington (1987), the lower limits imply that $n_e \lesssim 3 \times 10^6 \text{ cm}^{-3}$ if $T < 60,000$ K. The lines at $\lambda 4942$ and $\lambda 4989$ are contaminated by the strong complex of [O III] $\lambda\lambda 4959, 5007$, with the result that interesting constraints on T and n_e cannot be obtained from these lines (Keenan & Norrington 1991).

Overall, the above results point to a relatively high density for the narrow-line gas, which suggests a circumstellar rather than interstellar origin. If the [O III] and [Fe VII] lines are assumed to come from gas with similar physical properties, the implied characteristics are $n_e \approx 2 \times 10^6 \text{ cm}^{-3}$ and $T \approx 20,000$ K, although there is some evidence that the [Fe VII] emission comes from a somewhat hotter region. It is likely, because of the low velocity and the relatively low pressure, that this gas is the unshocked circumstellar wind. Presumably it was photoionized by the UV and X-ray radiation emitted by the supernova right after shock breakout.

One can derive a lower limit to the radial distance of this gas by taking the product of the highest observed supernova ejecta velocity and the estimated age. As discussed below, the highest velocity is $\sim 10^4 \text{ km s}^{-1}$. The wind electron density in front of the shock then becomes

$$n_e = 5.0 \times 10^4 \left(\frac{\dot{M}}{10^{-4} M_\odot \text{ yr}^{-1}} \right) \left(\frac{v_w}{10 \text{ km s}^{-1}} \right)^{-1} \left(\frac{t}{1000 \text{ days}} \right)^{-2} \text{ cm}^{-3}, \quad (1)$$

where \dot{M} is the mass-loss rate from the progenitor star, v_w is the wind velocity, and it has been assumed that H and He are fully ionized. The reference value of \dot{M} chosen here is close to the highest values that have been observed for Galactic stars and to the strong radio emitter SN 1979C (e.g., Lundqvist & Fransson 1988). Either the progenitor star of SN 1995N was losing mass at an extraordinary rate, or the density of the observed gas is higher than the average density in the circumstellar wind.

The gas density is sufficiently high that the recombination and excitation time scales are less than the supernova age, and approximate equilibrium is expected. The ionizing source is the X-ray emission, which had an unabsorbed X-ray luminosity of $\sim 1 \times 10^{41} \text{ erg s}^{-1}$ in the 0.1–10 keV band during July 1996 – January 1998 (Fox et al. 2000). The *ASCA* observations give a temperature estimate of 9 keV if the emission is thermal (Fox et al. 2000). Models of X-ray nebulae have been presented by Tarter, Tucker, & Salpeter (1969) and Kallman &

McCray (1982). The latter models assume a constant density surrounding a central source and generally take $T = 10$ keV for the photoionizing source, but the calculations can be used to approximate the current situation, especially because the [Fe VII] lines are likely to be formed in a region optically thin to the ionizing continuum. The ionization properties depend on the ionization parameter, which can be defined as $\xi = L/nr^2$, where L is the luminosity of the ionizing source. Taking $L = 1 \times 10^{41}$ erg s $^{-1}$, $n = 2 \times 10^6$ cm $^{-3}$, and $r = 8.6 \times 10^{16}$ cm, we find $\log \xi = 0.8$, which is very close to the ionization parameter where Fe VII is expected, for a $T = 10$ keV source (Kallman & McCray 1982). A lower temperature for the continuum source would increase the estimated ξ for a fixed L . The gas temperature of this region in the photoionization models is $\sim 15,000 - 20,000$ K, consistent with the observations. This comparison provides support for the overall model and, in particular, for the estimated radial distance of the emitting region.

The intensity of the narrow lines gives another constraint on the physical conditions. The hydrogen lines are the best to use because there are no abundance uncertainties. While no narrow H I lines can be seen in the day 1007 Keck spectrum because of the strong broad component, the higher resolution day 1799 VLT spectrum clearly shows H α , H β , and H γ . For H β , we find a luminosity of 5.3×10^{36} erg s $^{-1}$ at 1799 days. If the emitting region is assumed to be at radius r with a thickness Δr and a covering factor f , we have

$$f \frac{\Delta r}{r} \approx 1.6 \times 10^{-3} \left(\frac{r}{1.3 \times 10^{17} \text{ cm}} \right)^{-3} \left(\frac{n_e}{10^6 \text{ cm}^{-3}} \right)^{-2}, \quad (2)$$

where the emissivity of H β has been taken for $T = 20,000$ K (Osterbrock 1989). Although the density is uncertain, it is clear that the observations imply a small filling factor.

Another indication of the small filling factor of the $n_e = 2 \times 10^6$ cm $^{-3}$ gas is the detection of a substantial X-ray flux by *ROSAT*. If the gas were pervasive at $r = 8.6 \times 10^{16}$ cm, the resulting hydrogen column density, $N_H \approx 10^{23}$ cm $^{-2}$, would give rise to the complete absorption of the soft X-ray flux. The gas is not fully ionized and thus can effectively absorb the X-ray emission. In their estimate of the X-ray luminosity, Fox et al. (2000) take $N_H = 0.8 \times 10^{21}$ cm $^{-2}$ based on the expected Galactic absorption.

Most of the other ions that are observed in SN 1995N require an ionization parameter that is similar to that of Fe VII. The ions Fe VI through Fe XI, which are observed, occur over a relatively small range of ionization parameter (e.g., Kallman & McCray 1982). However, the presence of narrow [O I] emission implies the existence of a separate, lower-ionization component. The region could be of low ionization because of an especially high density, but it is more likely that the region is neutral because the ionizing photons have been used up in the H II region.

3.2. Intermediate Component

The intermediate-width component is best exemplified by the [O III] $\lambda\lambda 4959, 5007$ (Figure 5), [O II] $\lambda\lambda 7320, 7330$, and [O I] $\lambda\lambda 6300, 6363$ emission lines, which all show box-shaped profiles extending to $\sim 5,000 \text{ km s}^{-1}$. The strongest feature in this component at all epochs is the [O III] $\lambda\lambda 4959, 5007$ blend. Other likely members of this component are the high-ionization far-UV lines. Mg I] $\lambda 4571$ is a more uncertain member, showing a red deficit if it is correctly identified; alternatively, it could be a blend of lines, in particular [Fe II] $\lambda\lambda 4556, 4583$. The strongest argument for including Mg I] in this component is its temporal evolution, which is similar to that of the [O I] and [O III] lines (§ 5). There is no indication of hydrogen or helium with this type of profile.

Table 3 lists the fluxes of the lines that we designate as having line profiles coming from the intermediate component. As with the narrow lines, the intensity ratios of some of these lines provide constraints on the electron density and temperature.

O III. The [O III] $\lambda 4959$ and $\lambda 5007$ lines are strongly blended with each other, and the $\lambda 4959$ line with $H\beta$. A feature at $-1,800 \text{ km s}^{-1}$ appears in both the $\lambda 5007$ and $\lambda 4959$ lines, and the ratio of line strengths appears to be consistent with the 3:1 ratio expected from their spontaneous emission probabilities. The red edge of the $\lambda 5007$ line extends to $5,000 \text{ km s}^{-1}$, but not further. The $\lambda 5007$ line also has a strong feature to the red at $+3,000 \text{ km s}^{-1}$; however, it does not appear in [O III] $\lambda 4363$ or in other lines of this kinematic component, so there is a question of whether the feature originates from [O III] or is a blend. Its rapid drop in the late-time spectra (see § 5) argues for the blend interpretation. Likely candidates for this feature are He I $\lambda 5049$ or [Fe II].

Broad [O III] $\lambda 4363$ emission is present, although the blue side of the line is disturbed by $H\gamma$ emission. Neglecting the red feature in the $\lambda 5007$ line, we find $I(\lambda 5007 + \lambda 4959)/I(\lambda 4363) \approx 8.2$ from the day 1007 Keck spectrum. In the far-UV, the [O III] $\lambda\lambda 1660, 1666$ intercombination lines are among the strongest UV lines. Based on the wavelength, it is unlikely that the He II $\lambda 1640$ line contributes much to this feature. We find a reddening-corrected ratio [O III] $I(\lambda\lambda 4959, 5007)/I(\lambda\lambda 1660, 1666) \approx 4.0$.

O II. The [O II] $\lambda\lambda 7320, 7330$ doublet is less affected by blending and yields a clearer line profile. The feature at $-1,800 \text{ km s}^{-1}$ is present, but that at $+3,000 \text{ km s}^{-1}$ is not. The line profile is asymmetric, although the maximum velocity is $4,500 \text{ km s}^{-1}$ to both the blue and the red. As we show in § 4.1, the asymmetry is mainly caused by blending with He I $\lambda 7281$.

O I. The [O I] $\lambda\lambda 6300, 6364$ doublet is severely affected by the blue wing of $H\alpha$. Narrow components of the [O I] doublet, as well as [Fe X] $\lambda 6374.5$, also complicate the profile. In § 4

we show that the line profile is compatible with that of the other oxygen lines. The auroral [O I] $\lambda 5577$ line is likely to be present, although it may be distorted by the corresponding night-sky line. We therefore only consider its flux as an upper limit.

The presence of the O I recombination line at $\lambda 7774$ is of special interest because it should be accompanied by strong H I recombination emission with the same line profile, if the emission is from material with “cosmic” abundances, since hydrogen is more abundant than oxygen by a factor of 10^3 in such material. The absence of the corresponding hydrogen emission suggests that the emitting gas is oxygen rich. The O I recombination line at $\lambda 8446$, which is expected to have a strength comparable to the $\lambda 7774$ line, is blended with Fe II lines, and is also affected by fluorescence (§ 4.2). The emission may be from the oxygen-rich ejecta in the supernova and may extend to relatively high velocity because of hydrodynamic instabilities with the overlying layer (Fryxell et al. 1991) and/or a high expansion velocity of the oxygen core (§ 6.1).

The lines observed in the short-wavelength G160L *HST* spectrum are noisy, so there is uncertainty in the line identifications. The line widths, $\pm(3500 - 4000)$ km s $^{-1}$, point to memberships of most of the UV emissions with the intermediate kinematic component. The line profiles of the strongest lines (C IV, O III, and Si III/C III) are all consistent with flat-topped profiles of width ± 3800 km s $^{-1}$. Except for the $\lambda 1900$ feature, which has a central peak, the lines appear symmetric within the noise level. The C IV and Si IV lines are also affected by interstellar absorption in the Galaxy and the host galaxy.

By far the strongest line is Ly α , whose profile is distorted by geocoronal Ly α , and possibly by N V $\lambda 1240$. The C IV $\lambda\lambda 1548, 1551$ doublet is clearly seen with a boxy profile. The same is true for the feature at $\lambda 1900$, which can be identified as a blend of Si III] $\lambda 1892$ and C III] $\lambda\lambda 1907, 1909$. The N III] $\lambda\lambda 1744-1754$ lines are clearly present, although their flux is uncertain. The N IV] $\lambda 1486$ line is near the limit of detection.

In Figure 6 we show the density and temperature constraints from all the oxygen-line ratios of the *HST* and Keck day 1007 spectra together. We have used a reddening correction $E_{B-V} = 0.11$ mag to obtain $I([\text{O I}] \lambda 7774)/I([\text{O II}] \lambda\lambda 7320, 7330) = 0.43$, $I([\text{O III}] \lambda\lambda 4959, 5007)/I(\lambda 4363) = 8.2$, and $I([\text{O III}] \lambda\lambda 4959, 5007)/I(\lambda 1664) = 4.0$. The [O I] $I(\lambda 5577)/I(\lambda\lambda 6300, 6364)$ ratio is only an upper limit, $\lesssim 0.1$, and the curve shown in Figure 6 therefore only marks an upper boundary to the temperature. Implicit in this analysis is that the O I and O III zones are of similar extent, temperature, and electron density. While the lines coming from the O II and O III zones are all compatible with $T \approx 7000$ K and $n_e \approx 3 \times 10^8$ cm $^{-3}$, the [O I] lines have to arise in a lower temperature and/or lower electron density zone. As shown in Chevalier & Fransson (1994, hereinafter CF94), both these alternatives are quite natural, because the [O I] lines are expected to arise in a

partially neutral zone of lower temperature (see, e.g., CF94 Figures 4 and 5).

The velocities observed in the intermediate component suggest that this emission is from freely expanding ejecta. The ejecta are photoionized by X-rays from the circumstellar interaction. This process has been modeled by CF94, and there is general agreement between the lines that are predicted to be brightest and those that are observed here.

3.3. Broad Component

Because of the strong $H\alpha$ line, the broad component dominates the optical emission from the supernova. The total luminosity in $H\alpha$ was $\sim 2.3 \times 10^{40}$ erg s^{-1} on day 1007, using $E_{B-V} = 0.11$ mag. The line profile of $H\alpha$ is shown in Figure 5. There is no obvious distinction of different components in $H\alpha$, as we demonstrate in § 4.1, and no clear evidence for any velocity structure within the line, although a slight emission deficit can be seen on the red side of the line. The FWHM of the line is ~ 1600 km s^{-1} on day 1007. The wings are very extended and reach at least 10,000 km s^{-1} .

Table 4 gives a list of the lines that have profiles similar to that of $H\alpha$, although we can trace the high-velocity wings above ~ 3000 km s^{-1} only for $H\alpha$. Besides $H\alpha$, the best-defined line profile from this component is He I $\lambda 5876$, which is very similar to $H\alpha$ up to ~ 3000 km s^{-1} , where the line is lost in the noise. The broad component is dominated by lines of H I, He I, Mg II, and Fe II.

The interpretation of the Mg II $\lambda\lambda 2796, 2803$ doublet is complicated by absorption features arising in gas in our Galaxy and in the host galaxy of SN 1995N. The line peak is at negative velocities, at ~ 2791 Å, which may be a result of resonance-line scattering of the $\lambda 2796$ photons by the $\lambda 2803$ component, as well as the influence of the interstellar absorption lines. The line appears considerably broader than $H\alpha$, and shows a clear deficit of emission to the red of line center (Fig. 5). As discussed in § 4.2, the extended profile is likely to be caused by blending with Mg I $\lambda 2852$ and with the strong Fe II resonance lines in this region of the spectrum, expected to be present on either side of the wings (multiplets 399, 391, 380 at ~ 2850 Å, and multiplet 373 at ~ 2770 Å), due to the $Ly\alpha$ fluorescence.

Although almost all of the many Fe II lines present are blended with each other, it appears that they belong to the broad kinematic component. The only reasonably isolated Fe II line is $\lambda 7155$, whose profile is well fitted by a scaled $H\alpha$ profile. In the optical spectra, the region 4000–5500 Å contains a large number of Fe II lines, often seen in supernovae and active galactic nuclei (AGNs; e.g., Filippenko 1989; Osterbrock 1989). Comparing with spectra of narrow-line Seyfert 1 galaxies such as I Zw 1 (Phillips 1976, 1977), and the

symbiotic star RR Tel (Crawford et al. 1999), we have identified members of Fe II multiplets 14, 27, 28, 27, 42, 48, 49, and 74 (Table 4). The lines listed in Table 4 are those that can be identified with reasonable certainty. Most of the other members of the multiplets are blended with strong lines. One should also note that the fluxes of all Fe II lines, with the possible exception of the $\lambda 7155$ line, are highly uncertain.

In the UV, the plateau between $\sim 2300 \text{ \AA}$ and $\sim 2800 \text{ \AA}$, except for Mg II, is dominated by Fe II resonance lines. Because of the extreme blending of lines, which creates a pseudo-continuum, we do not attempt any complete identification in this spectral region. We simply note that there are some distinct features such as Fe II $\lambda\lambda 2614-2631$ and Fe II $\lambda\lambda 2506, 2508$. The latter lines are of special interest, because they arise from cascades from highly excited levels, and are usually considered an indicator of fluorescence. Except for this, the UV part of the spectrum is similar to that of I Zw 1 (e.g., Fig. 2d in Laor et al. 1997).

In the near-IR, it is especially interesting to note that many of the features can only be identified with Fe II emission based on models of Ly α fluorescence of the transitions (Johansson & Jordan 1984; Penston 1987; Sigut & Pradhan 1998a). Sigut & Pradhan (1998b), who discuss this process in detail for AGNs, provide a detailed list of the predicted lines, yielding many identifications for SN 1995N. The best example of Ly α fluorescence is probably the feature at $\sim 9150 \text{ \AA}$, which is difficult to explain with other mechanisms. Based on other Paschen lines, a significant contribution of H I is unlikely, and He I lines are also excluded by similar arguments, as well as by their wavelengths. Another candidate, Mg II $\lambda\lambda 9218, 9244$, also has the wrong wavelengths. In § 4.2 we show explicitly how the inclusion of these lines improves the spectral fit.

Finally, we point out the very strong He I $\lambda 10830$ line in the VLT day 1769 spectrum, which is the only spectrum covering this region.

Although there are many lines observed with the high-velocity component, the only straightforward diagnostic of the physical conditions is given by the lack of forbidden-line emission. In the case of the broad-line regions of AGNs, this is taken to indicate a density $\gtrsim 10^9 \text{ cm}^{-3}$ (e.g., Osterbrock 1989). This should be taken with some caution, however, because the gas is only partially ionized by the hard X-rays (CF94); high-ionization lines like [O III] $\lambda\lambda 5007, 4959$ and C III] $\lambda 1909$ are therefore unlikely to be present. The only forbidden lines expected are [O I] $\lambda\lambda 6300, 6364$, which are suppressed relative to permitted lines for $n_e \gtrsim 10^7 \text{ cm}^{-3}$. As we discuss in § 4.1, the large H α /H β ratio, as well as the Ca II line ratios, strongly argue that $n_e \gtrsim 10^9 \text{ cm}^{-3}$, which is a likely lower limit for the broad component.

The emission is presumably from a radius that is similar to the radius of the narrow-line

emission, and the gas is thus exposed to a radiation field that is comparable to that of the narrow-line gas. The high density results in an ionization parameter that is a factor $\gtrsim 10^3$ smaller than that for the narrow-line gas, or $\log \xi \lesssim -2$. The result is low ionization of the gas, as observed. The ionization is much less than that in the broad-line regions of AGNs, where lines like C IV $\lambda 1549$ are observed.

4. SYNTHETIC SPECTRA

To determine abundances as well as deblend the most important lines of the intermediate and broad components, we have calculated synthetic spectra based on the combined UV-optical *HST*/Keck spectrum from § 2. The model we employ is a simple two-component model, with constant physical parameters and abundances in each of the components. The temperature, densities, and abundances are taken as input parameters. For each of the two components we assume a given emissivity profile with velocity. The emissivities of the H and He lines are given by Case-B recombination, except for $H\alpha$, which is multiplied by some factor to account for collisions and optical-depth effects. The He I $\lambda\lambda 3889, 7065$ lines are also adjusted by a common factor to account for optical-depth effects (see Osterbrock 1989, p. 105). All lines from metals are calculated as multilevel atoms for a given temperature and density. The ionization fractions for a given ionization stage (such as C III, N III, O III, and Si III) are assumed to be the same. The continuum is due to H I, He I, and He II bound-free and two-photon continua, consistent with the recombination lines. We do not attempt to include the many Fe II lines present, nor lines from the narrow component. The temperature and ionization are not calculated self-consistently, as in CF94, so only the relative line fluxes for a given ion, or group of ions, are testing the model. The model should therefore mainly be viewed as a diagnostic tool.

For the line profiles we adjust the variation of the emissivity with velocity so that a best fit is obtained (eq. 3). For spherical symmetry and for a velocity $V(r) = V_{\max}(r/R_{\max})$, the flux at wavelength λ is given by

$$F_\nu(\lambda) = 2\pi \int_x^R S(r)(1 - \exp[-\tau(r)])r dr, \quad (3)$$

where $S(r)$ is the source function and $\tau(r)$ is the optical depth. In the optically thin limit $S(r)[1 - \exp(-\tau)] \approx j(r)$, where j is the emissivity. The limits of integration are given by $x = ct(\lambda - \lambda_0)/\lambda_0$, and $R = V_{\max}t$, where V_{\max} is the maximum ejecta velocity and c is the speed of light. This characterization of the line profile is appropriate for freely expanding ejecta; free expansion is assumed in our synthetic spectral models. As discussed in § 6.1.3, this assumption may not apply to the broad component. In this case, the line profile should

be viewed as an empirical fit that is applied to the set of lines.

4.1. Results

We find that the profile of the H I, He I, Mg II, and Fe II lines can be well reproduced with an emissivity [or, if $\tau \gg 1$, a source function $S(r)$] which is constant inside 1000 km s^{-1} and decreasing like $j(V) \propto V^{-4.6}$ outside, out to about $15,000 \text{ km s}^{-1}$. For the metal lines, except for Mg II and Fe II, we have used a constant-emissivity shell with $j = \text{constant}$ for $2500 < V < 5000 \text{ km s}^{-1}$.

In Figure 7 we show the spectrum of a model where all elements, including H, He, and metals, have the same density and temperature, $4 \times 10^6 \text{ cm}^{-3}$ and $14,000 \text{ K}$. The total metallicity is close to solar. Note that the temperature, density, and metallicity are only indicative, and depend on the assumed total emissivity, $\int n_e n r^2 dr$. The fit gives a good general representation of most lines, in terms of both the relative fluxes and line profiles. In particular, many of the profiles that seem fairly complicated at first sight are well reproduced as a result of blends by several lines. Good examples are the [O I] + H α complex, and the [O III] + H β feature at $4800\text{--}5000 \text{ \AA}$. The model, however, severely underproduces the strength of the important O I $\lambda 7774$ recombination line.

This could have been anticipated already from Figure 6, which shows that the relative [O III] ratios can be reproduced either with a high-temperature, low-density model, as in Figure 7, or with a low temperature and a high density. The [O II] $\lambda\lambda 7320 + 7330$ /O I $\lambda 7774$ ratio can, however, only be reproduced with the latter temperature/density combination. The relative fluxes of the oxygen and hydrogen/helium lines then require a very high oxygen abundance, unless the O II and O III zones are unreasonably large compared to the zone responsible for the H I and He I recombination lines. For the same extent, the relative flux in O I $\lambda 7774$ and H I lines is given by $[j_{\text{eff}}(\text{O I } \lambda 7774)n(\text{O II})]/[j_{\text{eff}}(\text{H I})n(\text{H II})]$. Because $j_{\text{eff}}(\text{O I } \lambda 7774) \approx 2 \times j_{\text{eff}}(\text{H}\beta)$, this shows that $n(\text{O II})$ and $n(\text{H II})$ must be of the same order of magnitude.

As an alternative, we show a model with a greatly increased metal abundance (Fig. 8). Although these lines are likely to arise in different ionization zones, we find that we can get an acceptable fit to all lines with a density $\sim 3 \times 10^8 \text{ cm}^{-3}$ and a temperature $\sim 7,000 \text{ K}$. All metal lines, except Mg II and Fe II, are assumed to have a shell-like emissivity profile. Compared to Figure 7 we see that, because of the high oxygen abundance, now both [O II] $\lambda\lambda 7320, 7330$ and O I $\lambda 7774$, as well as the strengths relative to the H I lines, are well reproduced. In addition, the O I $\lambda 8446$ recombination line contributes appreciably to

the feature at $\sim 8450 \text{ \AA}$. We also note the good fit to the O I $\lambda 7774$ line profile, further strengthening this identification.

To reproduce the observed $H\alpha/H\beta$ ratio, the $H\alpha$ strength has to be increased by a factor of ~ 8 above recombination. The reddening-corrected $Ly\alpha/H\alpha$ ratio is ~ 2.3 , while the Case-B ratio is ~ 24 . The flux of $Ly\alpha$ is, however, highly uncertain, because the line profile is disturbed by geocoronal $Ly\alpha$, in spite of the recession velocity of SN 1995N. As the self-consistent models in CF94 show, this occurs because of collisional excitation in combination with a high optical depth for $H\alpha$ in the partially ionized zone. As both the calculations in CF94 and similar models for AGNs (e.g., Kwan & Krolik 1981) show, this requires the presence of hard X-rays from the shocked region in combination with a density $\gtrsim 10^8 \text{ cm}^{-3}$. The higher-order Balmer lines are well explained by Case-B recombination.

The helium lines are well reproduced by pure recombination, except for He I $\lambda 3889$ and He I $\lambda 7065$. The former is down by a factor of ~ 0.5 , and consequently the He I $\lambda 7065$ line is increased by a factor of $2.0 \times 7065/3889 \approx 3.6$, which strongly indicates that the He I $\lambda 3889$ line is optically thick (e.g., Osterbrock 1989, p. 105).

The relative ratio of the He I and H I fluxes results in a He II/H II abundance of ~ 0.35 by number. Because the He II and H II ionization zones are likely to coincide (e.g., CF94), the He II/H II ratio is probably close to the elemental He/H abundance ratio. Strong He I lines are also present in SN 1986J (Rupen et al. 1987; Leibundgut et al. 1991) and at early times in many SNe IIn (e.g., Filippenko 1997).

The jump at $\lambda \approx 3700 \text{ \AA}$ is mainly caused by high-order Balmer lines and the Balmer continuum. The two-photon continuum dominates in most of the UV, as well as in the optical. The form of the Balmer continuum is sensitive to the temperature in the zone where this is formed, and a somewhat better fit is obtained for $T \approx 9000 \text{ K}$. In a one-zone model, however, this temperature gives a worse fit to the metal lines. More detailed models (CF94) show that both temperature and ionization vary within the emitting regions.

The Ca II lines in the spectrum are interesting. The IR triplet lines at $\lambda\lambda 8498, 8542, 8662$ are clearly present, while for the H&K lines and the forbidden $\lambda\lambda 7291.5, 7323.9$ lines we can only set upper limits. Fransson & Chevalier (1989) and Ferland & Persson (1989) have discussed the relative strengths of these lines as a function of density and temperature. Using their results we find that the fact that $I(\lambda\lambda 7291.5, 7323.9)/I(\lambda\lambda 8498, 8542, 8662) < 0.25$ and $I(\text{H\&K})/I(\lambda\lambda 8498, 8542, 8662) < 0.12$ means that the density must be $\gtrsim 10^9 \text{ cm}^{-3}$. This result is only weakly sensitive to the temperature.

The parts of the spectrum which are not well fitted by the model can in most cases be identified with regions of strong Fe II emission. This includes the UV between 2300 – 3000

Å, some regions in the range 4200 Å to 5300 Å, the $\lambda 7155$ line, and the fluorescence lines above ~ 8000 Å (see below).

In Figure 9 we show the line profiles and fits of the $H\alpha$, [O I], [O II], and [O III] lines to illustrate the fits for our assumed radial emissivity model. The figure also demonstrates the complex spectrum which results from the blending of the individually fairly simple line profiles.

Turning now to the other metal lines coming from the intermediate-velocity component, the UV line-intensity ratios require $N/C = 2.5-5$ and $O/N = 3.5-4.7$, by number. The high N/C ratio, in combination with the relatively large O/N ratio, strongly indicates incomplete CNO processing in this component.

While the profiles of the high-ionization C, N, O, and Si lines in the far-UV are consistent with the same shell-like emissivity as the oxygen lines, this emissivity model shows a bad fit of the Mg II $\lambda\lambda 2796, 2803$ line. The peaked profile shows that this line is instead likely to originate in the H and He-rich broad-line component, rather than in the metal-rich component.

4.2. Fe II – Ly α fluorescence

Based on the Fe II – Ly α fluorescence calculation by Sigut & Pradhan (1998a,b), we have modeled the near-IR spectrum of SN 1995N. We have used the same model as in Figure 8, but now added the Fe II lines, with wavelengths and fluxes from the list of Sigut & Pradhan. The line profiles were assumed to be the same as that of $H\alpha$. In the upper panel of Figure 10 we show the resulting spectrum, while in the lower panel we show for comparison the spectrum without Fe II lines. The observations are from the day 1769 VLT spectrum, but the day 716 and 1037 Lick spectra show the same features. The day 1007 Keck spectrum only extends to ~ 9000 Å.

As can be seen, there is a striking improvement with the observed features between 8000 Å and 9500 Å when the Fe II lines are included. In particular, the feature at ~ 9150 Å can be identified with the Fe II $\lambda\lambda 9071, 9128, 9177$ lines, and provides a good fit both in wavelength and profile of the blend.

One of the strongest expected fluorescence-pumped Fe II lines is at $\lambda 8451$, and there is indeed a strong feature at this wavelength. Another possible identification for this feature is the recombination line of O I $\lambda 8446$. This line is normally accompanied by O I $\lambda 7774$, which is not present in the broad component (although it is visible in the intermediate component;

see § 4.1). The recombination contribution to the $\lambda 8446$ line is expected to be close to the $\lambda 7774$ line, and is therefore insufficient to explain this strong feature. The $\lambda 8446$ line can be produced by fluorescence through the $\text{Ly}\beta$ line (Grandi 1980). Leibundgut et al. (1991) identified the O I $\lambda 8446$ line in the spectrum of SN 1986J. The $\text{Ly}\beta - \text{O I } \lambda 8446$ fluorescence also results in a strengthened O I $\lambda 1300$ multiplet. Due to its narrowness, however, this is likely to be absorbed by the O I in the host galaxy. In our Keck day 1007 spectrum of SN 1995N, the center of the emission feature gives a better match to Fe II $\lambda 8451$ than to O I $\lambda 8446$. An additional argument in favor of this mechanism is that Fe II $\lambda\lambda 2506, 2508$, which is indicative of $\text{Ly}\alpha$ pumping, is the strongest Fe II feature in the UV. This has previously been seen in η Carina, RR Tel, and KQ Pup (Baratta, Cassatella, & Viotti 1995; Johansson & Jordan 1984; Redfors & Johansson 2000). Other lines in the UV expected to be enhanced by fluorescence are the Fe II multiplets 399, 391, and 380 at 2850 \AA , multiplet 373 at 2770 \AA , and multiplet 363 at 2530 \AA . These most likely contribute to the broad wings of the Mg II lines, but are too blended to be uniquely identified. IR lines at $\sim 1.7 \mu\text{m}$ are also expected to be strong (Johansson & Hamann 1993), but are outside our observed wavelength range.

Given that the model was intended for conditions in an AGN, the fit is surprisingly good. Only at $\gtrsim 9300 \text{ \AA}$ are there a few features (such as at $\sim 9573 \text{ \AA}$) which are not well reproduced, but the noise level at these wavelengths is considerable. One should also note that the relative strengths depend on the uncertain atomic data, as well as on the exact $\text{Ly}\alpha$ profile. In particular, the larger line width in SN 1995N compared with those assumed in the AGN calculation by Sigut & Pradhan (1998a,b) model can change the results appreciably. Sigut & Pradhan assumed a static $\text{Ly}\alpha$ profile with only damping included. An expanding medium means that the $\text{Ly}\alpha$ line can feed many more fluorescence channels, which is likely to enhance the fluorescence effects.

Finally, we note the strong He I $\lambda 10830$ line in the day 1769 spectrum. Although the region beyond $\sim 9300 \text{ \AA}$ becomes increasingly noisy, this feature clearly stands out above the noise level. Compared to the strength expected by pure recombination, it is enhanced by collisional excitation by a factor of ~ 8 , which is common in many objects (e.g., Osterbrock 1989, p. 111).

5. TIME EVOLUTION

In Figure 11 we show the evolution of the reddening-corrected $\text{H}\alpha$ luminosity with time on a linear-log scale. We see that the evolution can be well approximated with an exponential decay, $L(\text{H}\alpha) \propto \exp(-t/\tau)$, where $\tau = 460$ days. This is much longer than the ^{56}Co decay time scale, and we conclude that the circumstellar interaction is responsible for the longevity,

although there is no obvious explanation for this particular time dependence.

An efficient way of displaying the change of the spectrum with time is to plot the ratio of two spectra as a function of wavelength. In Figure 12 we show a running average taken over 2 Å of the day 1799 VLT and day 1007 Keck spectra. The presence of two separate components in the spectrum is apparent. While most of the spectrum has decreased by a factor of ~ 6 , the intermediate-component [O I], [O II], and [O III] lines only decreased by a factor of 2–3. The O I $\lambda 7774$ line shows a similar decrease, while the $\lambda 8450$ feature follows the H I lines, consistent with it being mainly due to Fe II fluorescence lines. In addition, Mg I] $\lambda 4571$ belongs to the class of slowly declining lines.

Relative to $H\beta$, the peak fluxes of the [O I] and [O II] lines increased by a factor of ~ 3 between 1997 and 1999, while the [O III] line increased by a more modest factor of ~ 1.6 between these observations. The [O III] $\lambda\lambda 4959, 5007/\lambda 4363$ ratio remained nearly constant at ~ 7.9 , while the O I $\lambda 7774$ /[O II] $\lambda\lambda 7320, 7330$ ratio decreased from ~ 0.43 to ~ 0.20 . Repeating the analysis in § 3.2 (Fig. 6), we find that the temperature in the oxygen-rich gas had not changed much, while the electron density decreased from $\sim 3 \times 10^8 \text{ cm}^{-3}$ to $\sim 1 \times 10^8 \text{ cm}^{-3}$. This is less than expected from a simple $n_e \propto t^{-3}$ law, but our analysis assumes that the relative sizes of the O II and O III zones remain constant, and that the temperatures and densities in these two zones are similar. Neither of these conditions is obviously satisfied. In addition, the supernova may be older than our estimate, and the uncertainties in the relative fluxes are considerable. Nevertheless, the behavior is qualitatively that expected for expanding ejecta.

In Figure 13 we show the relative change of $H\alpha$, [O I] $\lambda\lambda 6300, 6364$, [O II] $\lambda\lambda 7320, 7330$, and [O III] $\lambda\lambda 4959, 5007$ on a velocity scale. While the [O I] and [O II] line profiles changed by roughly the same factor over the whole velocity range, -5000 to $+5000 \text{ km s}^{-1}$, the red side of the [O III] line decreased by a large factor relative to the blue. The most conceivable reason for the rapid [O III] change is that blending with another line, decreasing similarly to the H I and He I component, causes the apparent decrease in the red wing. The most likely candidates for this are the He I $\lambda\lambda 5015, 5049$ and Fe II lines. The blue side behaved in a manner similar to the [O I] and [O II] lines. We therefore conclude that there is little change in the overall profiles of the oxygen lines. When comparing the width of the best-isolated [O II] line, we find a nearly constant blue extension, while the width on the red side decreased by $\sim 450 \text{ km s}^{-1}$ during this period.

The evolution of the $H\alpha$ line profile differs dramatically from that of the oxygen lines. As shown in the upper-left panel of Figure 13, the red wing up to $\sim 3000 \text{ km s}^{-1}$ decreased by almost a factor of 4 relative to the blue, with a maximum decrease at $\sim 1100 \text{ km s}^{-1}$. To further illustrate the different evolution of the wings of $H\alpha$, we have reflected the blue

component in the spectra from 1996 – 1999 (Fig. 14), so that the blue and red wings can be compared directly. The fluxes have been normalized to the same peak value. We see that the day 716 Lick spectrum (dashed lines) showed nearly identical red and blue wings. The day 1007 Keck spectrum (solid lines) shows a clear evolution in that for a given velocity the red wing decreased faster than the blue wing. This is even more pronounced in the 1999 VLT spectrum, where at $\sim 1500 \text{ km s}^{-1}$ the flux of the red wing is only $\sim 20\%$ that of the blue wing at the same velocity. Equivalently, for a given intensity the red wing has a much smaller extension. For example, at $\sim 10\%$ of the peak flux the blue wing extends to $\sim 1900 \text{ km s}^{-1}$, while the red wing only extends to $\sim 1080 \text{ km s}^{-1}$. Relative to the peak flux, the blue wing shows a steady increase in flux with time, while the red wing displays the opposite trend. Similar evolution is seen for both $\text{H}\beta$ and $\text{He I } \lambda 5876$, although the continuum contribution and line blending make it difficult to compare directly to $\text{H}\alpha$. Baird et al. (1998) have presented evidence that the line slowly narrows with time. We can therefore confirm this trend to the latest epochs. The $\text{H}\alpha/\text{H}\beta$ ratio in the 1999 spectra decreased somewhat relative to the 1997 and 1996 spectra. This is consistent with the decreasing density during this time interval.

The intensity ratio of the He I lines to the Balmer lines does not change much. The two He I lines least affected by blending, He I $\lambda\lambda 5876, 7065$, have almost the same ratio relative to $\text{H}\beta$ at all epochs, and are all reproduced with a relative He II/H II abundance of ~ 0.35 by number. Together with the similar line profiles, this argues for the fact that the He I and Balmer lines arise in the same region. Their relative flux should therefore reflect their abundance ratio.

In most cases the fluxes of the narrow lines are uncertain, especially in the day 1799 spectrum. For the strongest lines, like $[\text{O III}] \lambda 5007$ and $[\text{Fe VII}] \lambda 6087$, the decrease is by a factor of 5–10, with no systematic distinction between lines from different elements. Although the flux of the $[\text{O III}] \lambda 4363$ line is especially uncertain due to the underlying broad component, there is an indication for an increase in the $[\text{O III}] \lambda 5007/\lambda 4363$ ratio from ~ 4.1 to ~ 6.6 . However, because this ratio depends on both density and temperature, one cannot directly translate this into a unique change in either of these parameters.

6. DISCUSSION

6.1. Nature of the Emission Regions

The general scenario for the emission from SN 1995N and related supernovae (generally Type II_n) is interaction of the supernova ejecta with circumstellar gas. Our spectra of SN

1995N show that the interaction is complex, but that there is sufficient diagnostic information on the emission components to deduce some of the interaction details. All the emission components are likely to be heated and ionized by the energetic radiation from the interaction region.

6.1.1. *Narrow Lines*

Based on the unresolved line widths, the density of $\sim 2 \times 10^6 \text{ cm}^{-3}$, and the low filling factor, the narrow-line emission can be identified with clumps in the preshock circumstellar gas. The velocity is likely to be $< 50 \text{ km s}^{-1}$, typical of the circumstellar media of red supergiants.

6.1.2. *Intermediate Component*

The intermediate-velocity component is identified with unshocked supernova ejecta. The maximum velocity in this component suggests either that the reverse shock front has a minimum velocity of $\sim 5,000 \text{ km s}^{-1}$, or alternatively that the emission is coming from a component which is photoionized by the shock but only extends in abundance to this velocity. The fact that this component is only seen as dense, oxygen-rich gas makes it natural to identify it as processed gas from the core. Assuming that the oxygen core expands at $5,000 \text{ km s}^{-1}$, the typical oxygen density will be

$$n_{\text{O}} \approx 4.1 \times 10^5 f^{-1} \left(\frac{M_{\text{core}}}{2 M_{\odot}} \right) \left(\frac{V_{\text{core}}}{5000 \text{ km s}^{-1}} \right)^{-3} \left(\frac{t}{1000 \text{ days}} \right)^{-3} \text{ cm}^{-3}, \quad (4)$$

where f is the filling factor of this component in the core, and we have assumed an oxygen-dominated composition. With $f \approx 0.1$, as was the case for SN 1987A (e.g., Spyromilio & Pinto 1991), the density is of the same order as found from the [O III] and similar lines. We note that the density deduced from the models is based on the assumption that the temperatures and densities are the same in the O I, O II, and O III zones.

A velocity of $\sim 5,000 \text{ km s}^{-1}$ is high for the oxygen core of a Type IIP or Type IIL supernova, but in the range found in Type Ib/Ic supernovae, as well as in the Type IIb SN 1993J (e.g., Houck & Fransson 1996; Matheson et al. 2000). This is an important result because it is consistent with a picture where the progenitor has lost most of its hydrogen-rich envelope before the explosion.

6.1.3. Broad Component

While most of the hydrogen-rich gas comes from gas moving at velocities of $\lesssim 2000 \text{ km s}^{-1}$, there is a smooth extension to $\sim 10^4 \text{ km s}^{-1}$. Any model must explain the wide range of velocities for this component. In particular, the fact that there appears to be hydrogen-rich, cool gas moving at up to $10,000 \text{ km s}^{-1}$ implies that there are some regions where the shock region extends considerably beyond the reverse shock front.

To explain this, one may identify three main alternatives for the broad, hydrogen-rich component. The first possibility is that it comes primarily from unshocked, freely expanding ejecta, extending from low-velocity hydrogen in the core up to the maximum ejecta velocity. A second possibility is that it comes from shocked ejecta gas, behind the reverse shock. The final possibility is that it comes from shocked circumstellar gas, either in the form of clumps or a more uniform medium. Our synthetic spectral models in § 4 are appropriate for the first possibility.

Before discussing these possibilities, we note that the Ca II lines, the absence of forbidden lines, and the $\text{H}\alpha/\text{H}\beta$ ratio indicate a density $\gtrsim 10^9 \text{ cm}^{-3}$ for this component (§ 4.1). A further independent lower limit to the density can be obtained by considering the state of ionization in this gas. The luminosity in $\text{H}\alpha$ was $\sim 2.3 \times 10^{40} \text{ erg s}^{-1}$ on day 1007 (§ 3.3). Typically, the conversion efficiency from X-rays to $\text{H}\alpha$ is $\sim 1\%$ (CF94), indicating a total X-ray luminosity of $2 \times 10^{42} \text{ erg s}^{-1}$. This is much more than was observed by *ROSAT* (Fox et al. 2000), but as calculations for SN 1993J showed (Fransson, Lundqvist, & Chevalier 1996), almost all the X-ray emission can be absorbed in the ejecta and shocked gas, and only the hard X-rays escape the supernova. With this luminosity the ionization parameter on day 1007 is $\xi \approx 1 \times 10^2 (n/10^6 \text{ cm}^{-3})^{-1}$. For a uniform density, hydrogen-dominated envelope expanding at $\sim 10,000 \text{ km s}^{-1}$, the density is

$$n \approx 4.1 \times 10^5 f^{-1} \left(\frac{M_{\text{env}}}{1 M_{\odot}} \right) \left(\frac{V_{\text{env}}}{10,000 \text{ km s}^{-1}} \right)^{-3} \left(\frac{t}{1000 \text{ days}} \right)^{-3} \text{ cm}^{-3}. \quad (5)$$

Therefore, if the emission came from unshocked ejecta and $f \gtrsim 0.1$, the ionization parameter would be very high, $\xi \gtrsim 10$, and one would expect strong emission from ions like [O III] from this component, contrary to the observations. Instead, it is dominated by Mg II and Fe II emission, in addition to the H I and He I lines, characteristic of a partially ionized, high-density region (e.g., CF94). It is therefore unlikely to come from a uniform-ejecta component, and only if clumping of this component is very high ($f \lesssim 0.01$) is an ejecta origin likely. We therefore think the first possibility given above is unlikely.

The density in the broad component is much higher than that in the narrow-line component, but the temperature is expected to be only slightly smaller. The conclusion is that

the pressure in the gas is relatively high and one possibility is shocked circumstellar or ejecta gas. The gas pressure is $p/k = 2 \times 10^{13} n_9 T_4 \text{ cm}^{-3} \text{ K}$, where n_9 is the H density in units of 10^9 cm^{-3} and T_4 is the temperature in units of 10^4 K . The pressure generated by a shock front moving into gas with a density of 10^6 cm^{-3} is $p/k = \rho_o v_s^2/k = 1.5 \times 10^{14} v_{s3}^2 \text{ cm}^{-3} \text{ K}$, where v_{s3} is the shock velocity in units of 10^3 km s^{-1} . If the emission is from shocks moving into a medium with a density of this order, the required high density can easily be produced.

We can identify two possibilities for such a shocked gas: it could be either clumps caused by instabilities in the shocked ejecta behind the reverse shock, or clumpiness and instabilities of the shocked circumstellar medium. This is similar to the two scenarios discussed by Chugai & Danziger (1994) for SN 1988Z.

Shocked ejecta: This is a version of the scenario discussed for “normal” interacting supernovae like SN 1979C or SN 1993J (CF94; Fransson et al. 1996). The fact that the line profiles in SN 1995N are peaked as opposed to the boxy profiles seen in SN 1993J, however, makes it necessary to modify this scenario. One possibility is that the circumstellar medium is highly asymmetric, as in the picture discussed by Blondin, Lundqvist, & Chevalier (1996). Indications for a highly asymmetric circumstellar medium are seen in some red supergiants in a superwind phase (see § 6.2). Most of the hydrogen emission could in this case come from the cool, dense shell expected behind the reverse shock (CF94). The shape of the H α line profile then reflects the decreasing emission measure as one moves away from the equator. The maximum ejecta velocity is likely to occur at the poles, while the strongest interaction, with most of the energy release, occurs in the high-density circumstellar gas at the equator. The deceleration of the ejecta will therefore be most rapid here. If the hydrogen envelope mass is low, the reverse shock at the equator may rapidly recede to the massive oxygen core. This could qualitatively explain the presence of the high-ionization, oxygen-rich shell observed in the intermediate-component line profiles. The hydrogen-rich gas in the cool shell behind the reverse shock could then be excited by the X-rays from the shock, giving rise to an extended partially ionized zone. A prediction is that the maximum velocity of the shocks, and therefore the line widths, should decrease with time.

This general scenario for SN 1995N receives support from observations of the related supernova SN 1986J in NGC 891, which had a strong H α line with FWHM $\approx 700 \text{ km s}^{-1}$ and oxygen lines with widths of several 10^3 km s^{-1} (Leibundgut et al. 1991). It was a strong radio source, and VLBI images showed a shell with protrusions extending at least a factor of two beyond the shell radius (Bartel et al. 1989, 1991). Images on different dates revealed expansion; the outer protrusions are moving at $\sim 15,000 \text{ km s}^{-1}$, while the shell is expanding at $\sim 5,000 \text{ km s}^{-1}$. These images suggest a picture that is consistent with that deduced from the spectra of SN 1995N.

The origin of the protrusions is uncertain, but there are computational simulations that suggest that they could arise from asymmetries or inhomogeneities in the circumstellar medium. Blondin et al. (1996) found that supernova expansion into a circumstellar medium with a density deficit in the polar direction could produce polar protrusions with a radius 2–4 times that of the main shell. The problem in comparison to the images of SN 1986J is that there are more than two protrusions. Jun, Jones, & Norman (1996) carried out a simulation of the interaction of a supernova with a clumpy medium and found that the Rayleigh-Taylor instability that develops where the ejecta are decelerated by the surrounding medium is accentuated by the presence of clumps. The Rayleigh-Taylor fingers reach the outer shock front. The protrusions in the simulation did not reach the extent required for SN 1986J, but the simulation was run for a limited amount of time and the density of the surrounding medium was uniform. The circumstellar wind case remains to be investigated.

Shocked circumstellar clouds: In this scenario, the emission comes from the cool gas behind the slow radiative shocks propagating into the same clumpy gas clouds as are responsible for the narrow-line emission. The blast wave may then propagate in the intercloud medium, while the high-density circumstellar clumps are left behind. The maximum ejecta velocity will decrease only slowly, while the shocked clouds will be accelerated on a time scale which depends on the column density of the clouds. As simulations show (e.g., Klein, McKee, & Colella 1994; Jun et al. 1996), however, the cloud may gradually be evaporated, and finally be dissolved and merge with the ejecta gas. In this scenario one expects a smooth distribution of gas, with velocities ranging from newly shocked clouds with low velocity, or clouds with very high column density, to gas which has been accelerated to the ejecta velocity. This agrees qualitatively with the observed H α line profile. The observed gradual increase of the flux in the blue wing with time is also consistent with this scenario. The decrease in the red wing, however, is not naturally explained, unless it is caused by dust absorption, either from pre-existing dust in the circumstellar gas, or from newly formed dust in the ejecta, as discussed for SN 1998S by Gerardy et al. (2000).

6.1.4. *Location of the Energy Source*

An important question is the location of the energy source for the excitation of the gas, and there are several possibilities. First, the source could be the shock separating the high-velocity hydrogen ejecta from the circumstellar gas. In the uniform-medium case this will be at the highest velocity and also maximum ejecta radius. This is the model discussed by CF94, and applied to SN 1993J by Fransson et al. (1996). However, it is difficult to understand the presence of the high-ionization, oxygen-rich shell at only ~ 5000 km s $^{-1}$,

since most of the X-rays will be absorbed by the unprocessed ejecta between the shock and the oxygen core.

In the clumped circumstellar medium case the bow shocks may be distributed over a large radius, and immersed in the expanding ejecta, depending on the time of shocking and their column densities. The oxygen-shell emission is again difficult to explain. It may, however, explain the distributed nature of the hydrogen emission.

6.2. Type IIn Progenitors

Some clues to realistic scenarios for the structure of the circumstellar medium can be obtained from observations of Galactic supergiants in very advanced evolutionary stages. While most red supergiants, like α Ori, have fairly modest winds with mass-loss rates $\lesssim 10^{-5} M_{\odot} \text{ yr}^{-1}$, there is a handful of massive stars having more extreme mass-loss rates, $10^{-4} - 10^{-3} M_{\odot} \text{ yr}^{-1}$, often referred to as “superwinds.” Van Loon et al. (1999) find that two out of eight red supergiants in an LMC sample have mass-loss rates $\gtrsim 10^{-3} M_{\odot} \text{ yr}^{-1}$, while the others have moderate mass-loss rates $\lesssim 10^{-5} M_{\odot} \text{ yr}^{-1}$.

The best-studied superwind cases are VY CMa and IRC +10420. The nature of the superwind phase is not yet clear, but can be related either to a specific evolutionary phase, occurring for most red supergiants, or to a phase only occurring for a specific mass range. A hint that the latter is the case comes from the fact that both VY CMa and IRC +10420 are very luminous stars, with $L \approx (2 - 5) \times 10^5 L_{\odot}$. From evolutionary models Wittkowski, Langer, & Weigelt (1998) estimate a zero-age main sequence (ZAMS) mass of 30–40 M_{\odot} for VY CMa. The mass-loss rate is determined to be $\sim (2 - 3) \times 10^{-4} M_{\odot} \text{ yr}^{-1}$ for a wind velocity of 39 km s $^{-1}$ (Danchi et al. 1994).

Several authors have found an asymmetric distribution of the circumstellar gas and dust around VY CMa. From *HST* imaging Kastner & Weintraub (1998) find an asymmetric core region with wavelength dependent FWHM $\approx 10^{15}$ cm in the optical. The star itself has a radius of $\sim 1.2 \times 10^{14}$ cm. Outside of this is an asymmetric reflection nebula with an extent of $\sim 6 \times 10^{16}$ cm, with the core close to its edge. Based on symmetry arguments, Kastner & Weintraub speculate that this is only one half of a bipolar nebula, with the other half obscured by an opaque equatorial dust disk. The same conclusion is reached by Monnier et al. (1999) from high-resolution observations of the core and extended structure.

The supergiant IRC +10420 is similar to VY CMa in terms of mass-loss rate and mass, but probably in an even later evolutionary state, intermediate between a red supergiant and a Wolf-Rayet star. There is also evidence for a disk-like geometry in this case, based on line

profiles (Jones et al. 1993) and on *HST* and IR imaging (Humphreys et al. 1997).

Wittkowski et al. (1998) propose that the asymmetric mass loss arises as a result of rapid rotation in the phase preceding the evolution off the Hayashi line when the major part of the envelope is lost. VY CMa is now estimated to have a mass of $\sim 15 M_{\odot}$, meaning that it has lost $\sim 25 M_{\odot}$ to the circumstellar medium. The helium fraction at this phase is ~ 0.4 by mass. This is lower than, although qualitatively consistent with, our results for SN 1995N, but is obviously sensitive to mixing prescriptions, the exact evolutionary status, and other factors. As an alternative, Soker (2000) proposes that the asymmetric distribution is caused by the concentration of magnetic spots in the equatorial plane, which through the lower photospheric temperature causes dust formation preferentially at the equator.

Based on these cases, it seems probable that SN 1995N, and other Type II_n supernovae, arise from progenitors similar to VY CMa or IRC +10420. This is consistent with the high mass-loss rates needed to explain the strong interaction, as reflected in the total luminosity. A low hydrogen envelope mass is needed to explain the large oxygen core velocity. The observed high He/H ratio is also consistent with high mass loss. An asymmetric circumstellar distribution will result in faster expansion of the supernova ejecta in the polar directions, while it will be slowed down by the equatorial disk or torus as modeled by Blondin et al. (1996). The radius of the inner boundary of the dusty disk in VY CMa is estimated to be $\sim 10^{15}$ cm (Monnier et al. 1999). If the density in the disk is large enough, the radius of the inner edge would not be much affected by the supernova ejecta. The relative size of the ejecta and obscuring disk would therefore increase with time. If the disk is opaque due to dust, an increasingly large fraction of the ejecta on the far side of the supernova would be obscured. This could explain the fact that the red side of the $H\alpha$ line decreased considerably faster than the blue side. The exact temporal evolution depends on the degree of asymmetry of the ejecta.

Evidence for dusty environments comes from several Type II supernovae. Especially interesting are the observations of SN 1998S, where Gerardy et al. (2000) find strong evidence for dust emission. As Gerardy et al. discuss, although this dust could in principle be formed in the ejecta, perhaps a more likely interpretation is pre-existing circumstellar dust, heated by the supernova (see also Fassia et al. 2001).

From observations of H_2O masers in VY CMa, Richards, Yates, & Cohen (1998) estimate a density of $\sim 5 \times 10^9 \text{ cm}^{-3}$ in the masing regions, while other species give a density of $\sim 10^8 \text{ cm}^{-3}$, indicating a considerable clumpiness of the circumstellar medium. One then speculates that these masing regions could be related to the high-density clumps needed to decelerate the supernova blast wave.

Finally, the small fraction of supernovae in this class, $\lesssim 5\%$ (Cappellaro et al. 1993), is at least qualitatively consistent with them coming from a fairly small fraction of the high-mass stars.

7. CONCLUSIONS

Late-time spectral observations of SN 1995N are presented, covering the UV to near-IR regions. Three kinematic components are found, which most likely are powered by X-rays from the interaction of the ejecta and the circumstellar medium of the progenitor. Spectral modeling shows evidence of an increased helium abundance, as well as CNO burning. The first evidence for Ly α pumped fluorescence of Fe II lines in supernovae is found. It is likely that other supernovae interacting with their circumstellar media show similar signatures, especially in the near-IR. While the narrow lines come from unshocked circumstellar gas and the intermediate-velocity component from processed ejecta, the high-velocity unprocessed gas has a more uncertain origin. Different possibilities based on either clumpy or asymmetric circumstellar media are discussed, without strongly favoring either of these possibilities. The temporal evolution of the processed and unprocessed gas is distinctly different, again emphasizing the different origins of these components. We propose that the progenitors of the narrow-line supernovae (Type IIn) are similar to red supergiants in their superwind phase, as most of the hydrogen-rich gas is expelled in the last $\sim 10^4$ years before explosion. This explains the high oxygen core velocity. We also present evidence that the circumstellar medium is either asymmetric or clumpy.

We are grateful to Anil Pradhan and Aron Sigut for sending us their fluorescence results in detailed form. Financial support for this work was provided to A.V.F.’s group by NSF grants AST-9417213 and AST-9987438, by the Guggenheim Foundation, and by NASA through grants GO-6043, GO-6584, and GO-8602 from the Space Telescope Science Institute, which is operated by AURA, Inc., under NASA contract NAS 5-26555. Support was also provided to R.A.C. by NASA grant NAG5-8232, and to C.F.’s group by the Swedish Space Board and Swedish Research Council. Some of the data presented herein were obtained at the W. M. Keck Observatory, which is operated as a scientific partnership among the California Institute of Technology, the University of California, and NASA; the Observatory was made possible by the generous financial support of the W. M. Keck Foundation. We thank the staffs at the *HST*, ESO, Lick, and Keck Observatories for their overall assistance, as well as Andrea Gilbert, Jeff Newman, and Adam Riess for their help with some of the observations.

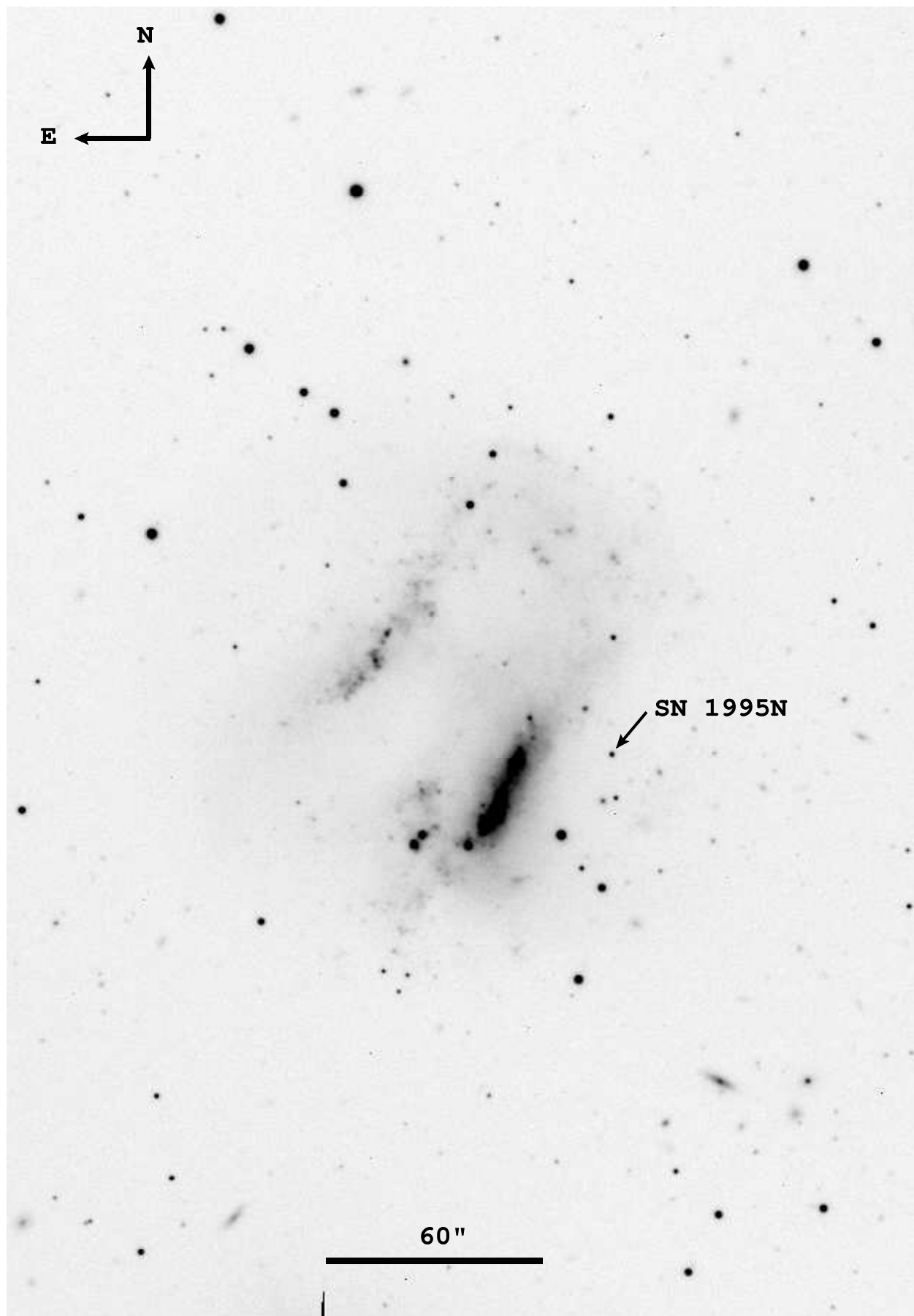
REFERENCES

- Aretxaga, I., et al. 1999, MNRAS, 309, 343
- Baird, M. D., Garnavich, P. M., Schlegel, E. M., Challis, P. M., & Kirshner, R. P. 1998, BAAS, meeting 193, paper 47.04
- Baratta, G. B., Cassatella, A., & Viotti, R. 1995, A&AS, 113, 1
- Bartel, N., Rupen, M. P., Shapiro, I. I., Preston, R. A., & Rius, A. 1991, Nature, 350, 212
- Bartel, N., Shapiro, I. I., & Rupen, M. P. 1989, ApJ, 337, L85
- Benetti, S., Bouchet, P., & Schwarz, H. 1995, IAU Circ. 6170
- Blondin, J. M., Lundqvist, P., & Chevalier, R. A. 1996, ApJ, 472, 257
- Cappellaro, E., Turatto, M., Benetti, S., Tsvetkov, D. Y., Bartunov, O. S., & Makarova, I. N. 1993, A&A, 268, 472
- Chevalier, R. A., & Fransson, C. 1994, ApJ, 420, 268 [CF94]
- Chugai, N. N. 1993, ApJ, 414, L101
- Chugai, N. N., & Danziger, I. J. 1994, MNRAS, 268, 173
- Chugai, N. N., Danziger, I. J., & Della Valle 1995, MNRAS, 276, 530
- Crawford, F. L., McKenna, F. C., Keenan, F. P., Aller, L. H., Feibelman, W. A., & Ryan, S. G. 1999, A&AS, 139, 135
- Danchi, W. C., et al. 1994, AJ, 107, 1469
- Fabian, A. C., & Terlevich, R. 1996, MNRAS, 280, 5P
- Fassia, A. et al. 2001, MNRAS, 325, 907
- Filippenko, A. V. 1989, AJ, 97, 726
- Filippenko, A. V. 1997, ARA&A, 35, 309
- Filippenko, A. V. 1991a, in Supernovae, ed. S. E. Woosley (New York: Springer-Verlag), p. 467
- Filippenko, A. V. 1991b, in Supernova 1987A and Other Supernovae, eds. I. J. Danziger & K. Kj ar (Garching: ESO), p. 343

- Filippenko, A. V. & Halpern, J. P. 1984, *ApJ*, 285, 458
- Ferland, G. J., & Persson, S. E. 1989, *ApJ*, 347, 656
- Fox, D. W., et al. 2000, *MNRAS*, 319, 1154
- Fransson, C., & Chevalier, R. A. 1989, *ApJ*, 343, 323
- Fransson, C., Lundqvist, P., & Chevalier, R. A. 1996, *ApJ*, 461, 993
- Fryxell, B., Müller, E., & Arnett, D. 1991, *ApJ*, 367, 619
- Galama, T. J., et al. 1998, *Nature*, 395, 670
- Garnavich, P., & Challis, P. 1995, *IAU Circ.* 6174
- Gerardy, C. L., Fesen, R. A., Höflich, P., & Wheeler, J. C. 2000, *AJ*, 119, 2968
- Grandi, S. A. 1980, *ApJ*, 238, 10
- Houck, J. C., Bregman, J. N., Chevalier, R. A., & Tomisaka, K. 1998, *ApJ*, 493, 431
- Houck, J. C., & Fransson, C. 1996, *ApJ*, 456, 811
- Humphreys, R. M., et al. 1997, *AJ*, 114, 2778
- Johansson, S., & Hamann, F. 1993, *Phys. Scr*, 18, 217
- Johansson, S., & Jordan, C. 1984, *MNRAS*, 210, 239
- Jones, T. J., et al. 1993, *ApJ*, 411, 323
- Jun, B.-I., Jones, T. W., & Norman, M. L. 1996, *ApJ*, 468, L59
- Kallman, T., & McCray, R. 1980, *ApJ*, 242, 615
- Kallman, T. R., & McCray, R. 1982, *ApJS*, 50, 263
- Kastner, J. H., & Weintraub, D. A. 1998, *AJ*, 115, 1592
- Keenan, F. P., & Norrington, P. H. 1987, *A&A*, 181, 370
- Keenan, F. P., & Norrington, P. H. 1991, *ApJ*, 368, 486
- Klein, R. I., McKee, C. F., & Colella, P. 1994, *ApJ*, 420, 213
- Kong, X., & Cheng, F. Z. 1999, *A&A*, 351, 477

- Kulkarni, S. R., et al. 1998, *Nature*, 395, 663
- Kwan, J., & Krolik, J. H. 1981, *ApJ*, 250, 478
- Laor, A., Jannuzi, B. T., Green, R. F., & Boroson, T. A. 1997, *ApJ*, 489, 656
- Leibundgut, B., Kirshner, R. P., Pinto, P. A., Rupen, M. P., Smith, R. C., Gunn, J. E., & Schneider, D. P. 1991, *ApJ*, 372, 531
- Leonard, D. C., Filippenko, A. V., Barth, A. J., & Matheson, T. 2000, *ApJ*, 536, 239
- Lundqvist, P., & Fransson, C. 1988, *A&A*, 192, 221
- Matheson, T., Filippenko, A. V., Ho, L. C., Barth, A. J., & Leonard, D. C. 2000, *AJ*, 120, 1499
- Miller, J. S., & Stone, R. P. S. 1993, Lick Observatory Technical Report, No. 66 (Univ. of California)
- Monnier, J. D., Tuthill, P. G., Lopez, B., Cruzalebes, P., Danchi, W. C., & Haniff, C. A. 1999, *ApJ*, 512, 351
- Nussbaumer, H., & Storey, P. J. 1982, *A&A*, 113, 21
- Oke, J. B., et al. 1995, *PASP*, 107, 375
- Osterbrock, D. E. 1989, *Astrophysics of Gaseous Nebulae and Active Galactic Nuclei* (Mill Valley, CA: Univ. Science Books)
- Penston, M. V. 1987, *MNRAS*, 229, 1P
- Phillips, M. M. 1976, *ApJ*, 208, 37
- Phillips, M. M. 1977, *ApJ*, 215, 746
- Pollas, C. 1995, *IAU Circ.* 6170
- Redfors, A., & Johansson, S. G. 2000, *A&A*, 364, 646
- Richards, A. M. S., Yates, J. A., & Cohen, R. J. 1998, *MNRAS*, 299, 319
- Rupen, M. P., van Gorkom, J. H., Knapp, G. R., Gunn, J. E., & Schneider, D. P. 1987, *AJ*, 94, 61
- Ryder, S., Staveley-Smith, L., Dopita, M., Petre, R., Colbert, E., Malin, D., & Schlegel, E. 1993, *ApJ*, 416, 167

- Schachter, J., Filippenko, A. V., & Kahn, S. M. 1990, *ApJ*, 362, 74
- Schlegel, E. 1990, *MNRAS*, 244, 269
- Schlegel, D. J., Finkbeiner, D. P., & Davis, M. 1998, *ApJ*, 500, 525
- Schlegel, E. M., Petre, R., & Colbert, E. J. M. 1996, 456, 187
- Sigut, T. A. A., & Pradhan, A. K. 1998a, *ApJ*, 499, L139
- Sigut, T. A. A., & Pradhan, A. K. 1998b, private communication
- Soker, N. 2000, *MNRAS*, 312, 217
- Spyromilio, J., & Pinto, P. A. 1991, in *Supernova 1987A and Other Supernovae*, eds. I. J. Danziger & K. Kj ar (Garching: ESO), p. 423
- Stathakis, R. A., & Sadler, E. M. 1991, *MNRAS*, 250, 786
- Tarter, C. B., Tucker, W. H., & Salpeter, E. E. 1969, *ApJ*, 156, 943
- Theureau, G., Bottinelli, L., Coudreau-Durand, N., Gouguenheim, L., Hallet, N., Louergue, M., Paturel, G., & Teerikorpi, P. 1998, *A&AS*, 130, 333
- Turatto, M., Cappellaro, E., Danziger, I. J., Benetti, S., Gouiffes, C., & Della Valle, M. 1993, *MNRAS*, 262, 128
- Van Dyk, S. D., Sramek, R. A., Weiler, K. W., Montes, M. J., & Panagia, N. 1996, *IAU Circ.* 6386
- Van Dyk, S. D., Weiler, K. W., Sramek, R. A., & Panagia, N. 1993, *ApJ*, 419, L69
- van Loon, J. T., Groenewegen, M. A. T., de Koter, A., Trams, N. R., Waters, L. B. F. M., Zijlstra, A. A., Whitelock, P. A., & Loup, C. 1999, *A&A*, 351, 559
- Weiler, K. W., Panagia, N., & Sramek, R. A. 1990, *ApJ*, 364, 611
- Wittkowski, M., Langer, N., & Weigelt, G. 1998, *A&A*, 340, L39



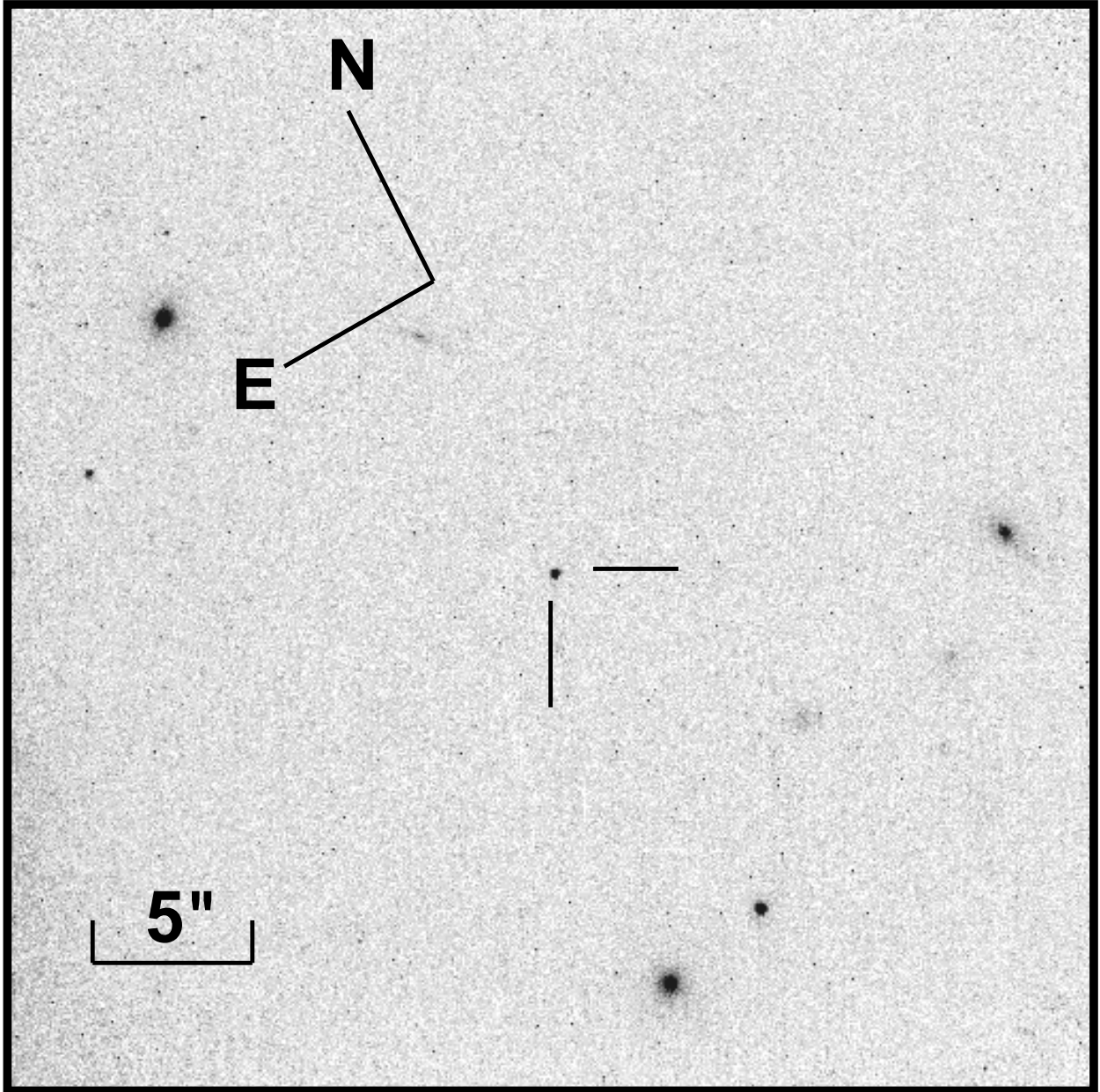


Fig. 2.— *HST* PC F814W image of SN 1995N from 22 July 2000. The SN has $I \approx 20.5$ mag.

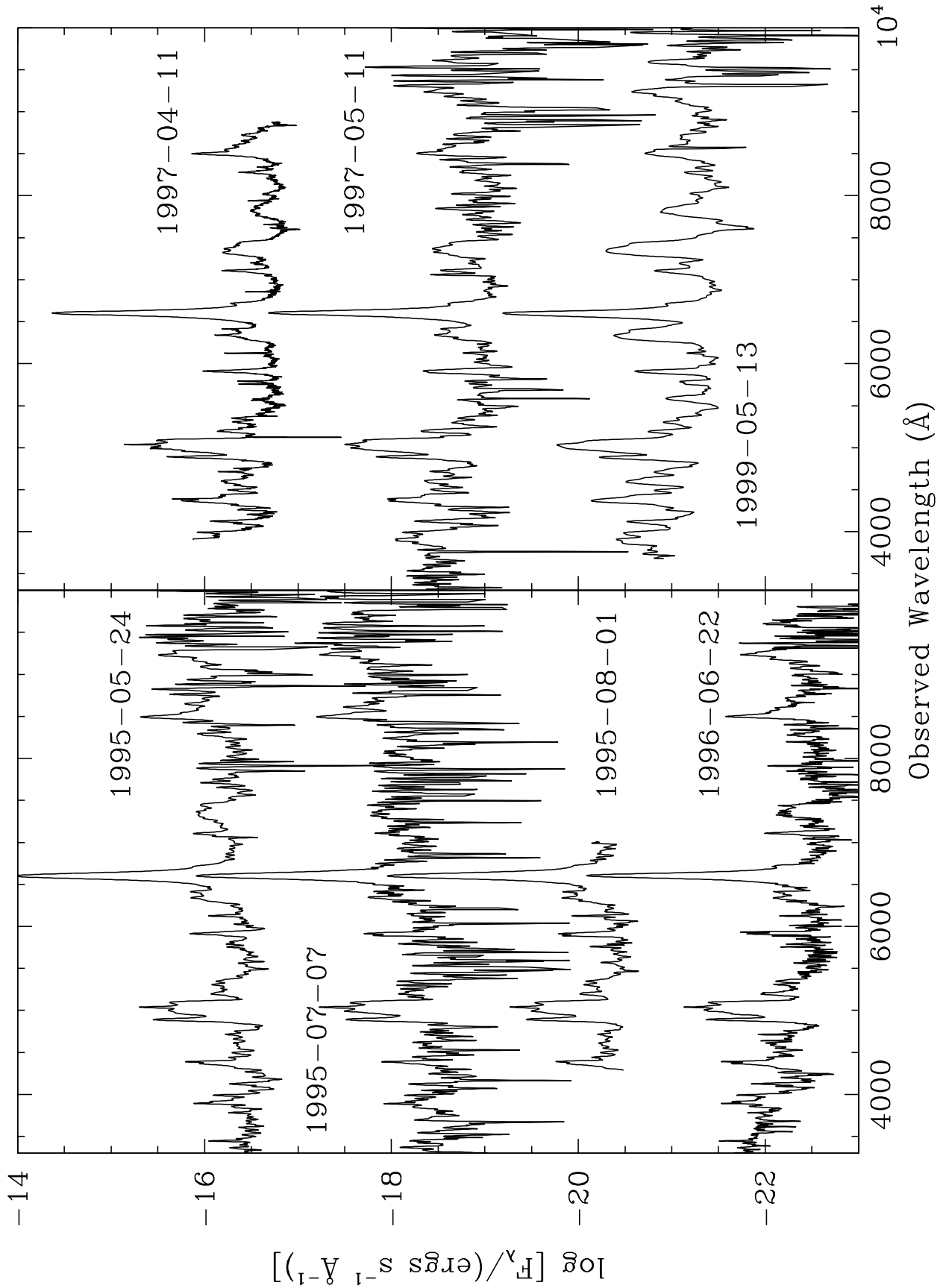


Fig. 3.— Spectra of SN 1995N within 5 years after discovery. All except the 11 April 1997 Keck spectrum and the 13 May 1999 VLT spectrum were obtained with the Lick 3 m Shane

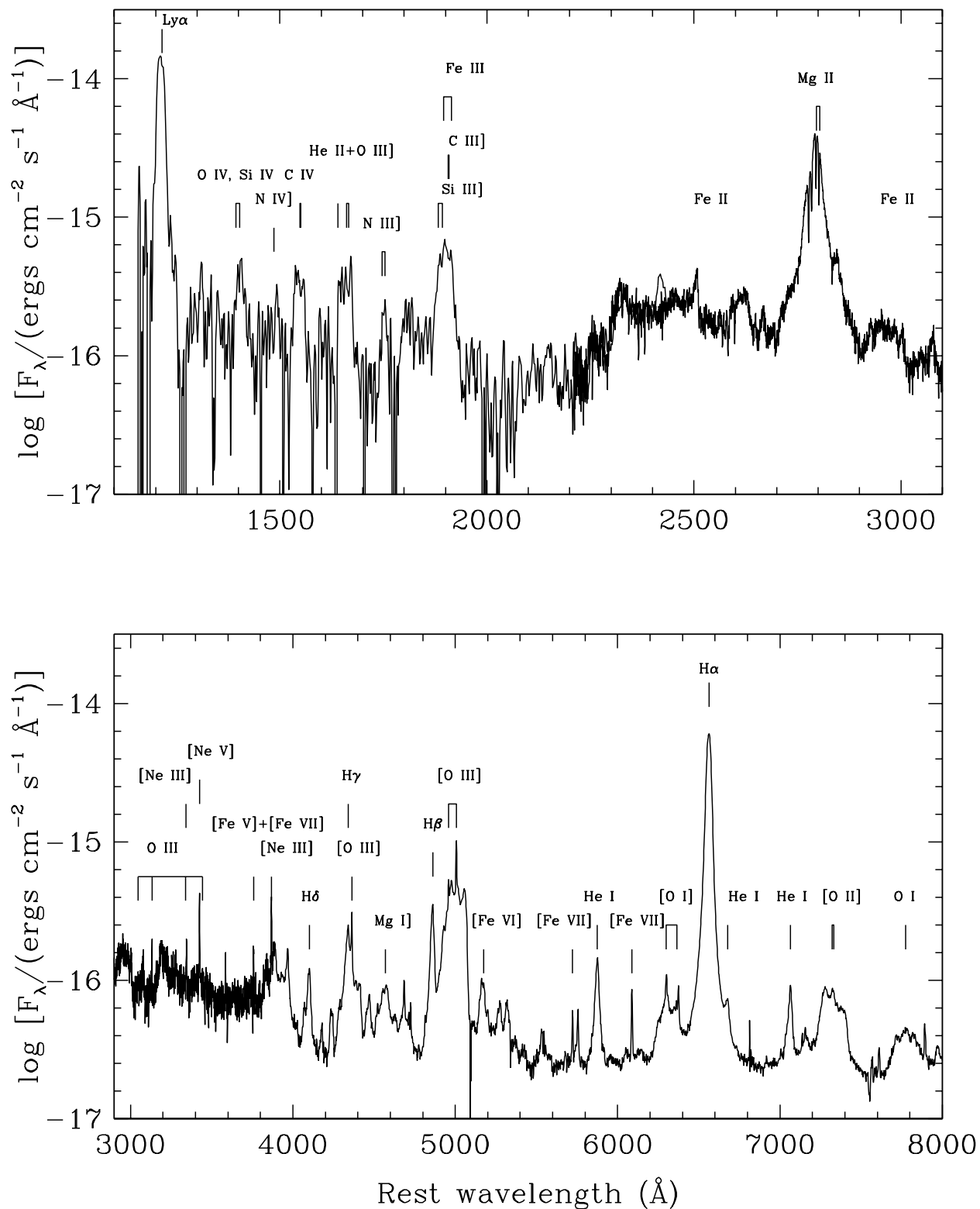


Fig. 4.— Combined day 943 (*HST*) and day 1007 (Keck) spectra of SN 1995N, with identifications of the strongest lines. We have omitted identifications of the many Fe II lines in the UV and visible ranges. Wavelengths are in the rest frame of the supernova.

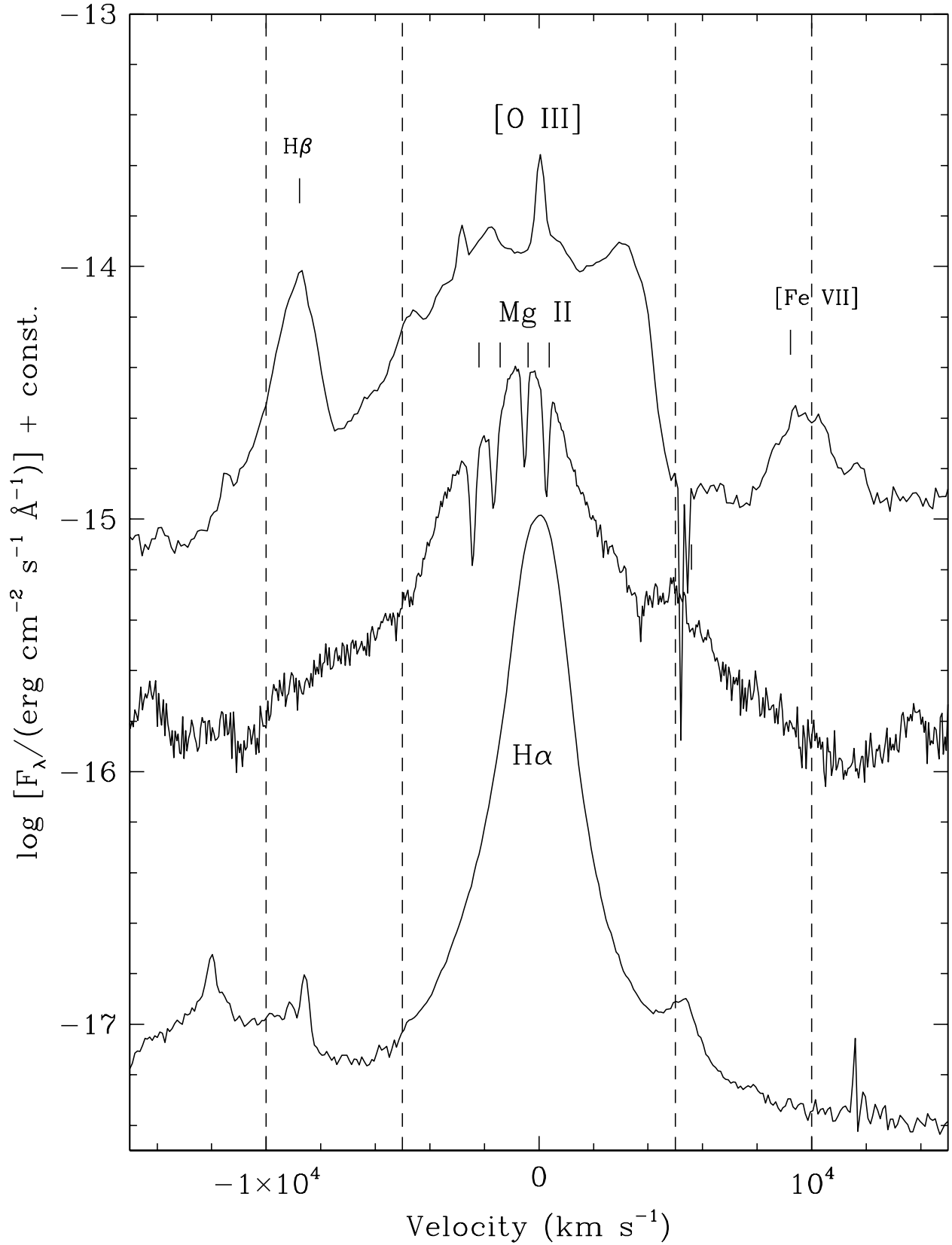


Fig. 5.— Line profiles of Mg II $\lambda\lambda 2796, 2803$, [O III] $\lambda\lambda 4959, 5007$, and H α .

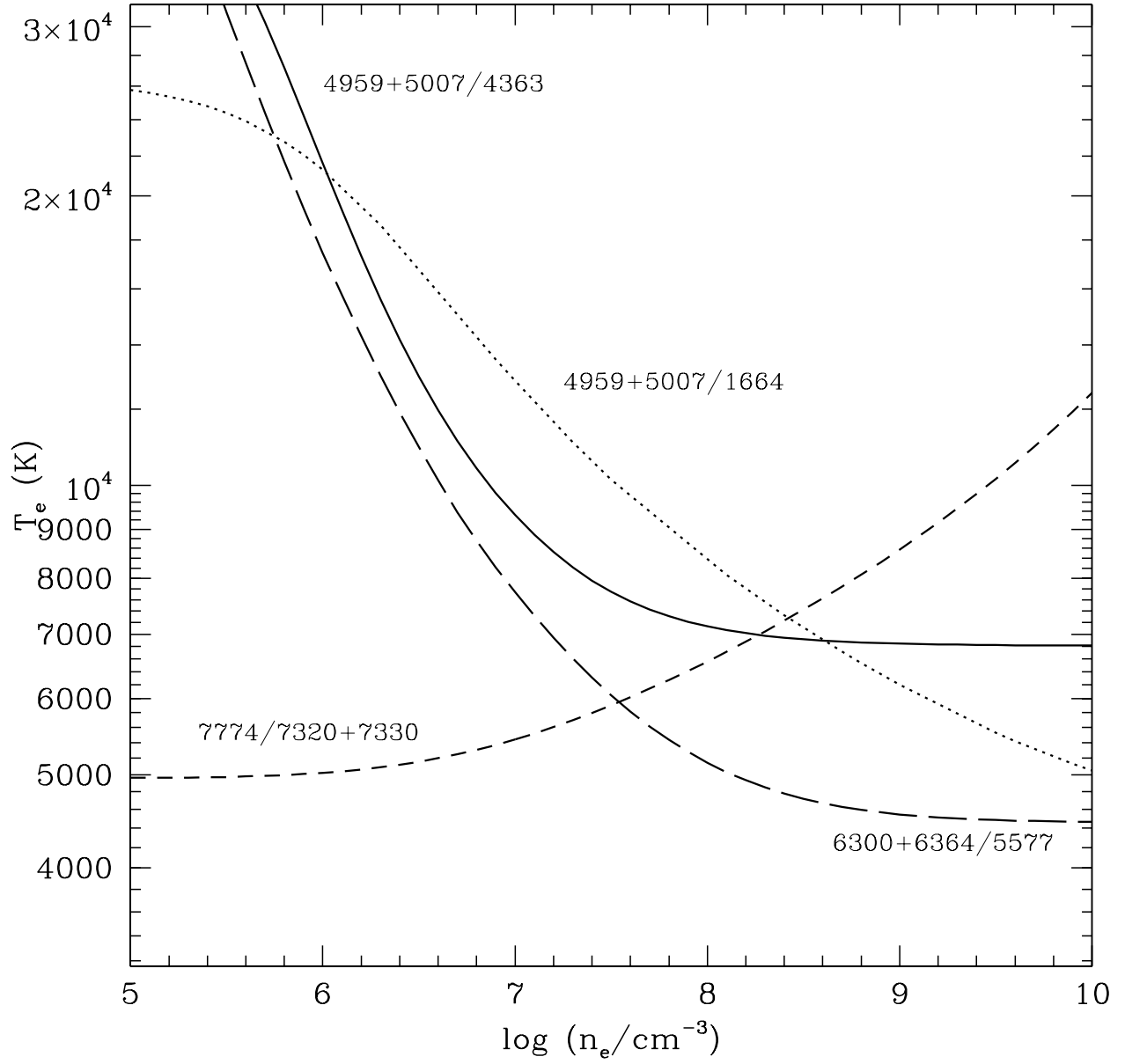


Fig. 6.— Temperature vs. density plot for the oxygen lines. The [O I] $\lambda\lambda 6300, 6364/\lambda 5577$ curve marks only an upper limit to the temperature for a given electron density.

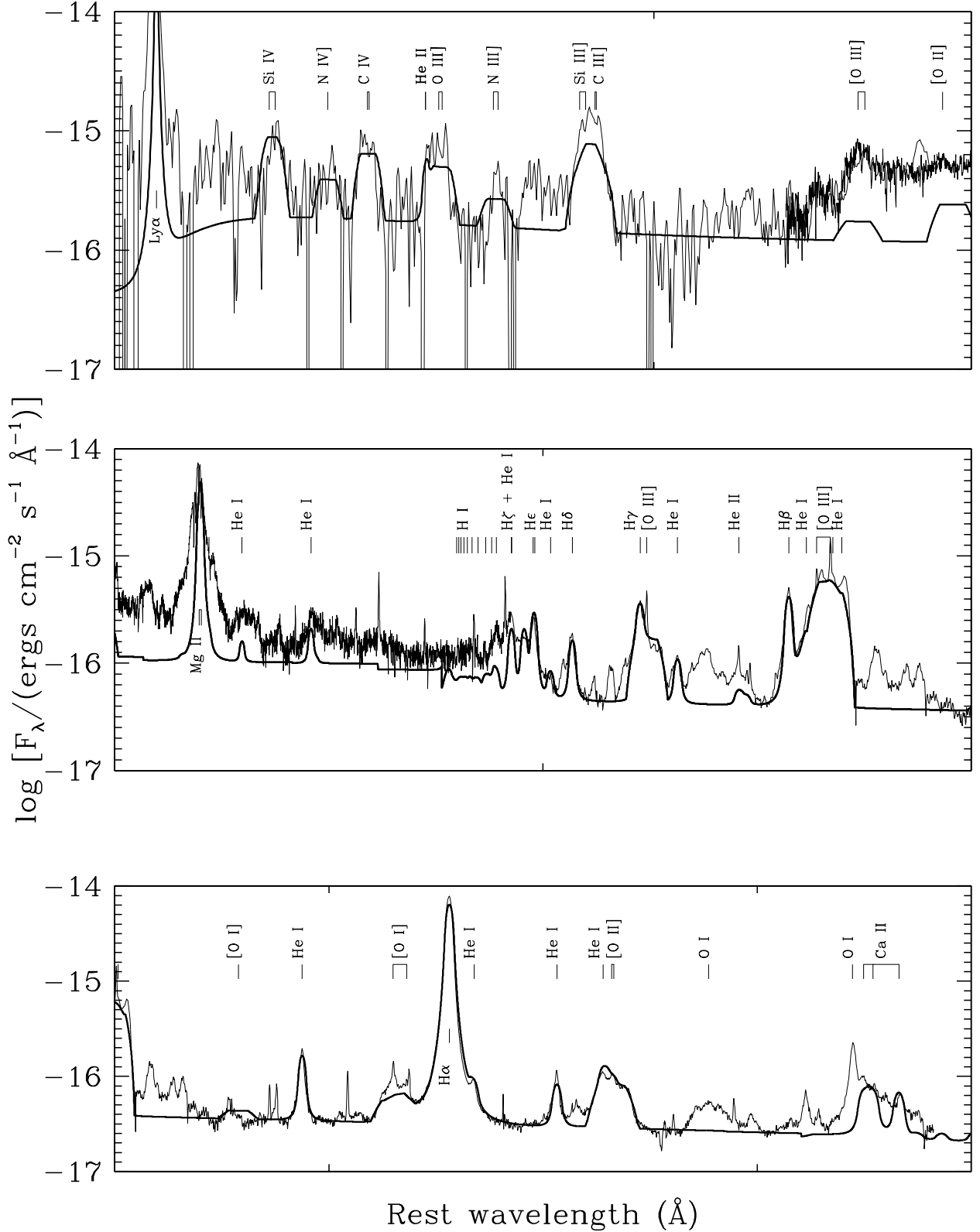


Fig. 7.— Synthetic spectrum superimposed on the day 1007–1037 spectra, corrected for reddening. The model includes H, He, C, N, O, Mg, Si, and Ca, but no Fe II lines. The metallicity is close to solar, $T = 14000$ K, and $n_e = 4 \times 10^6 \text{ cm}^{-3}$. Note the severe underproduction of O I $\lambda 7774$, caused by the normal metallic abundances.

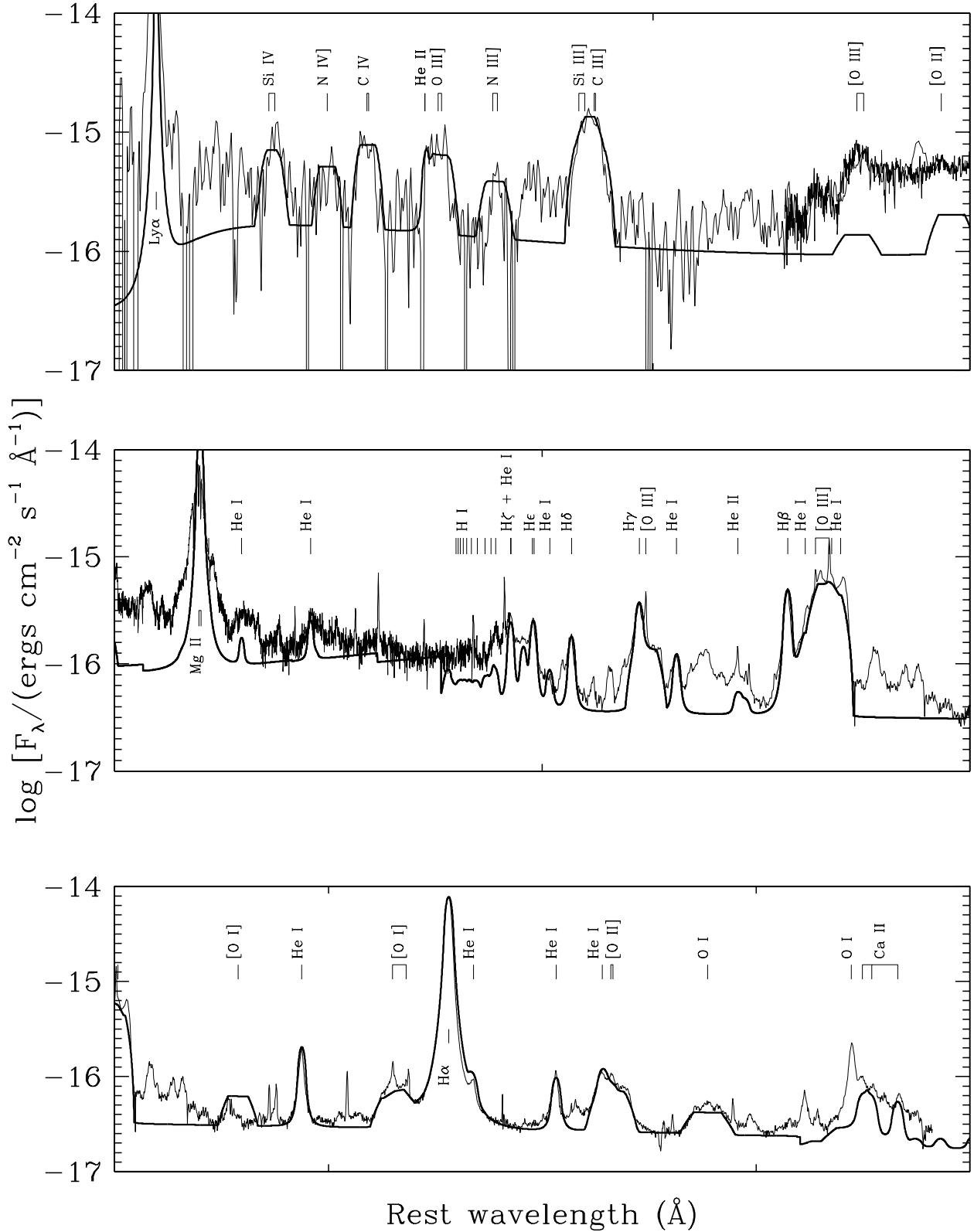


Fig. 8.— Same as Fig. 4, but now with $T = 7500$ K, $n_e = 3 \times 10^8 \text{ cm}^{-3}$, and a high metal abundance. The O I $\lambda 7774$ line is now well-reproduced relative to the other O I and O II lines.

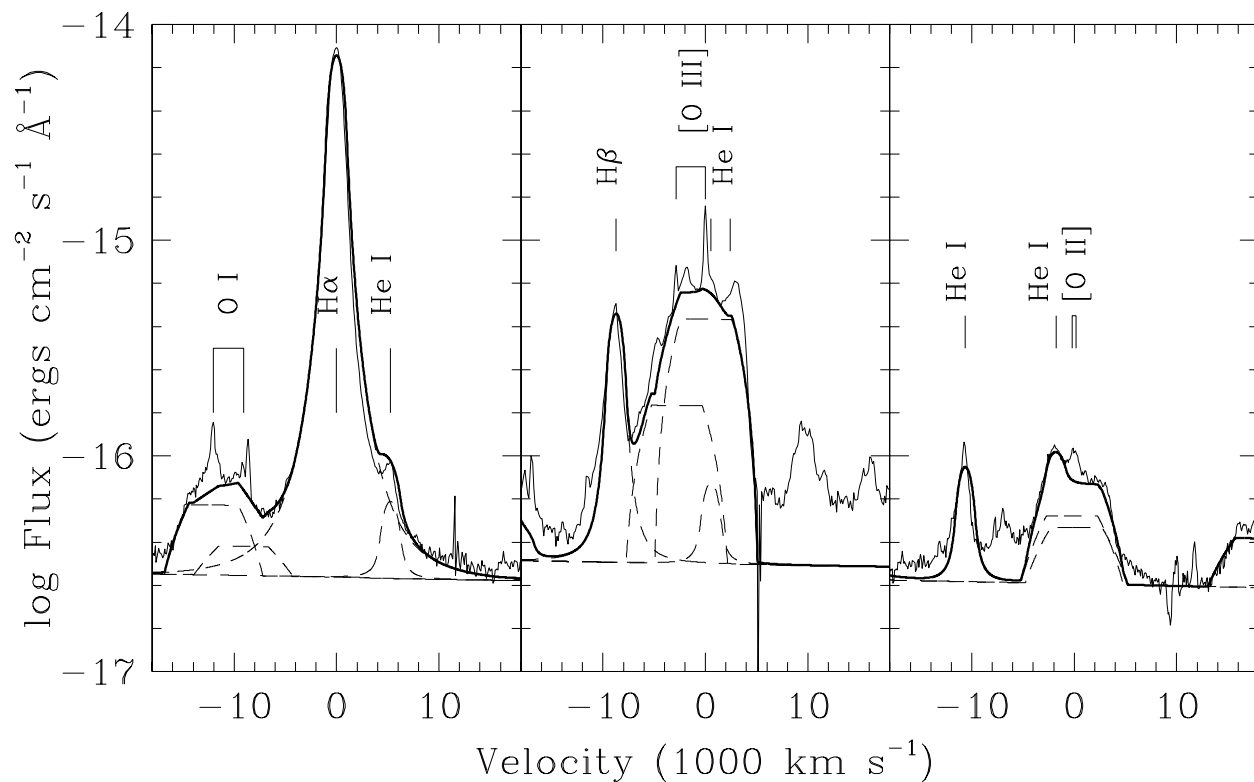


Fig. 9.— Spectral fit and decomposition of the $H\alpha$, [O I], [O II], and [O III] line profiles from the day 1007 spectrum. The velocity scale is counted from $H\alpha$, [O III] $\lambda 5007$, and [O II] $\lambda 7325$, respectively. The dashed lines give the most important separate contributions to the total line profile. The narrow components of the [O I], [O II], and [O III] lines are apparent as the excess emission.

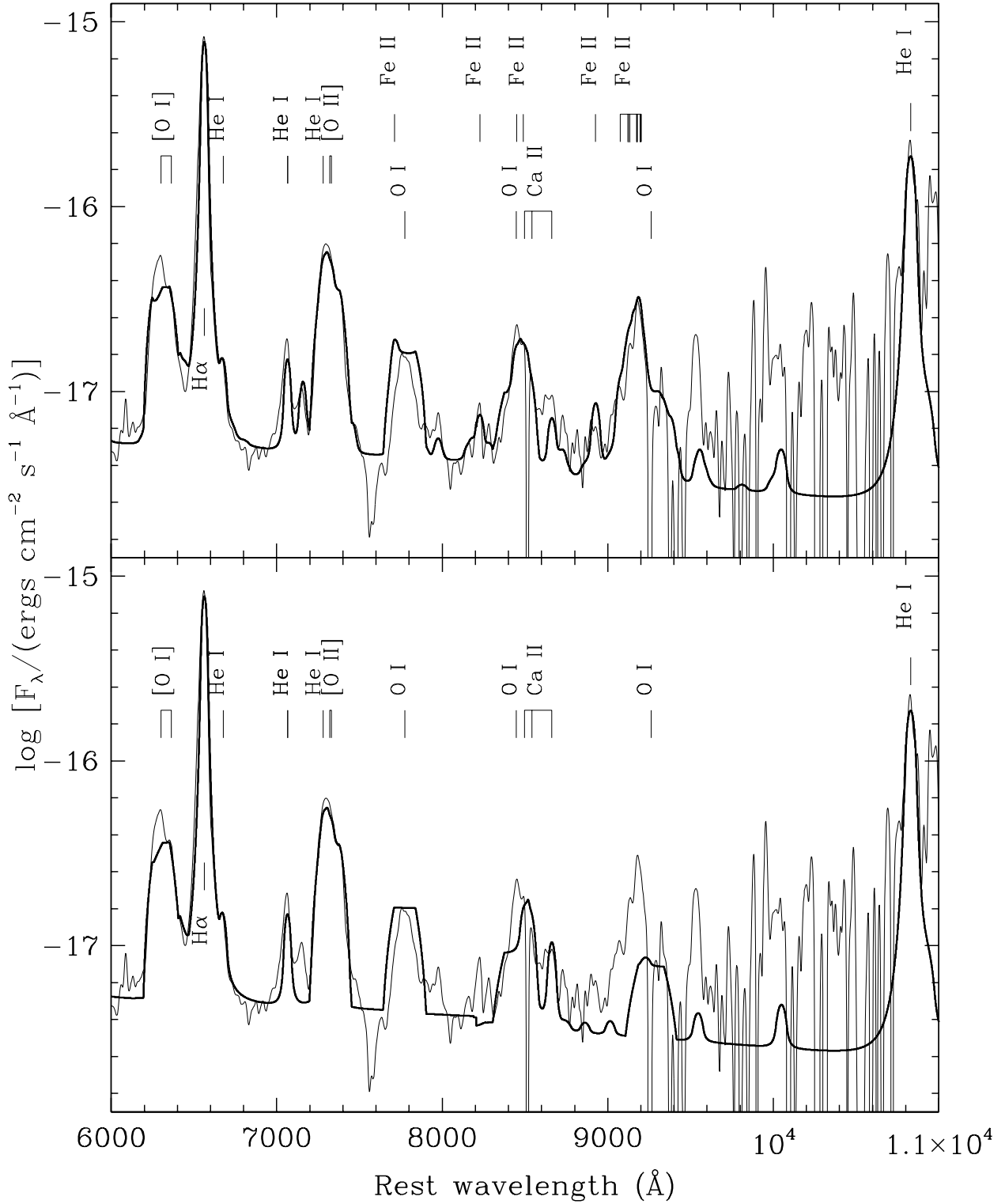


Fig. 10.— The observed near-IR region of the spectrum of SN 1995N on day 1769, together with the synthetic spectrum expected based on the Ly α fluorescence mechanism (thick line). The upper panel includes the Ly α fluorescence, while the lower does not. Note especially the greatly improved fits at $\sim 8500 \text{\AA}$ and $\sim 9150 \text{\AA}$. Also note the strong He I $\lambda 10830$ line.

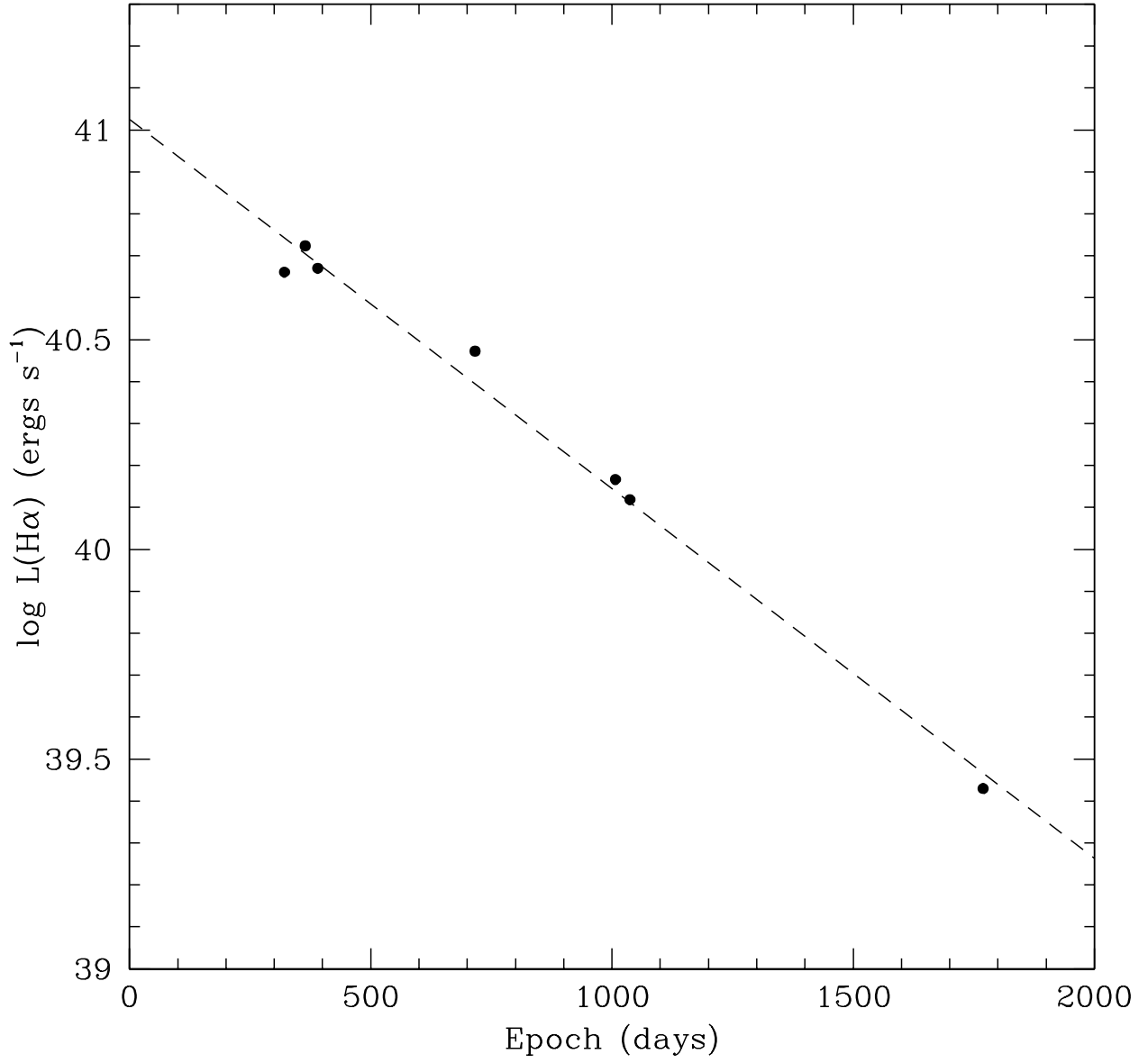


Fig. 11.— Evolution of the H α luminosity with time. The dashed line gives a least-squares fit to the data.

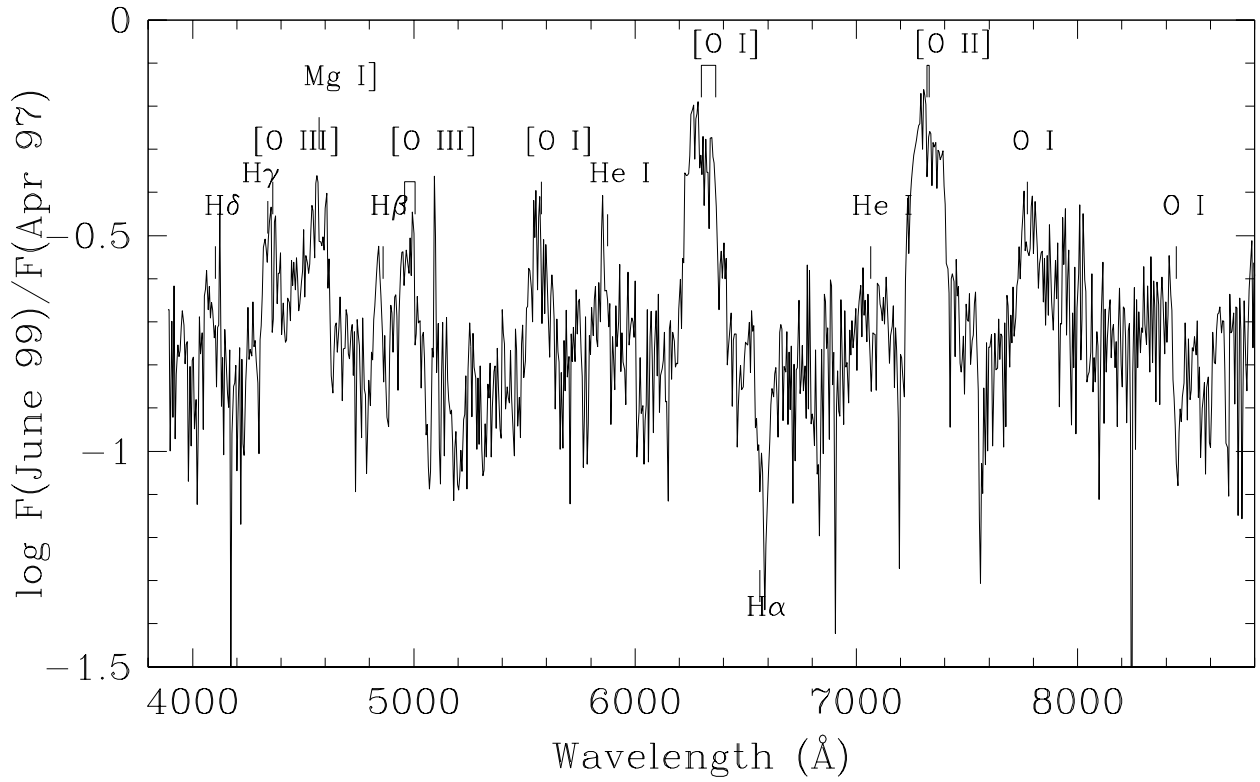


Fig. 12.— Ratio of the day 1799 and day 1007 spectra with identifications of the most important lines. Note the peaks of the [O I], [O II], [O III], and Mg I lines, showing that these belong to a component separate from the H I, He I, and Fe II lines.

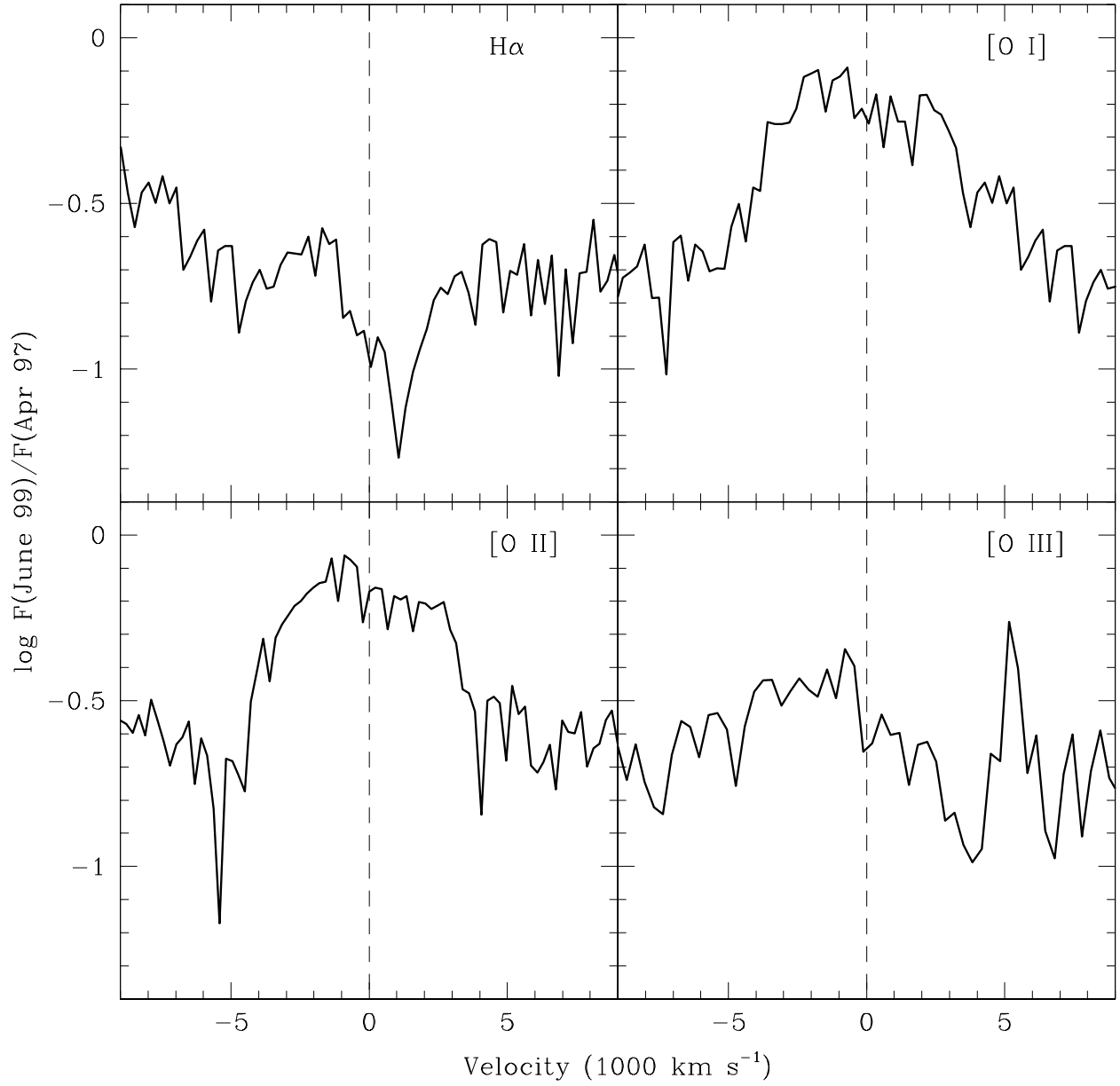


Fig. 13.— Ratio of the day 1799 and day 1007 spectra for $\text{H}\alpha$, $[\text{O I}]$, $[\text{O II}]$, and $[\text{O III}]$.

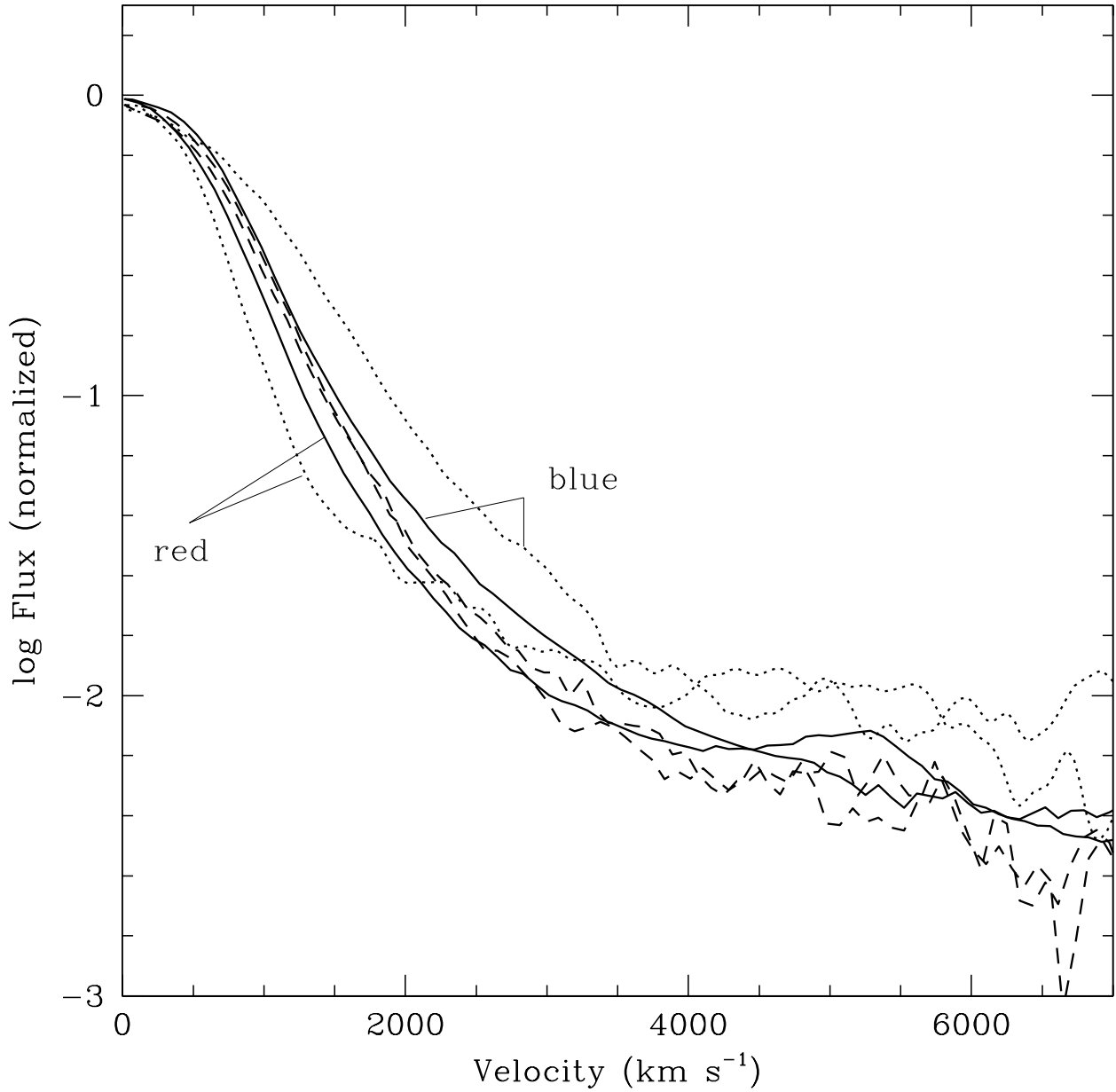


Fig. 14.— Evolution of the H α line profile from 1996 (Lick; dashed line), to 1997 (Keck; solid line), to 1999 (VLT; dotted line). Note the strong decrease in the red wing of the line relative to the blue wing in the 1997 and 1999 spectra.

Table 1. Log of observations

UT Date	Epoch ^a days	Telescope	Wavelength Range (Å)	Resolution (Å)
24 May 1995	321	Lick 3 m	3120 – 10490	6–11
6–7 July 1995	364–365	Lick 3 m	3120 – 10490	6–11
1 August 1995	390	Lick 3 m	4260 – 7040	6
22 June 1996	716	Lick 3 m	3120 – 9880	6
6 February 1997	943	HST	1140 – 4780	2–7
11 April 1997	1007	Keck I	3910 – 8880	10
16 April 1997	1012	Lick 3 m	3160 – 9870	6
11 May 1997	1037	Lick 3 m	3120 – 9880	6–11
13 May 1999	1769	VLT	3635 – 11680	13
12 June 1999	1799	VLT	3908 – 9187	5

^aBased on an assumed explosion date of 4 July 1994.

Table 2. Fluxes of narrow lines

Line	Rest wavelength (Å)	Observed wavelength (Å)	Flux ^a				Notes
			22 June 1996	6 Feb 1997	11 April 1997	12 June 1999	
[Fe XI]	7891.8	7891.9			1.2	0.12	
?		7610.3			0.81	0.17	
[Ar III]	7135.8	7135.7			0.26	0.12	
He I (n)	7065.3	7065.5				0.11	
[Ar V]	7005.7	7005.0			0.21		broad?
H α	6562.8	6563.8			\lesssim 2.1	0.78	
[Fe X]	6374.5	6375.5	1.8		1.3		
[O I]	6363.8	6363.0			0.47		
[O I]	6300.3	6301.0	3.0		3.0	0.22	
[Fe VII]	6087.0	6086.8	3.7		2.8	0.60	
[N II]	5754.6	5755.5			2.2		broad?
[Fe VII]	5720.7	5721.9	3.0		1.6	0.7	
[Fe VI]	5677.0	5677.5			0.50		
[Fe VII]+[Fe VI]	5276.4+5277.8	5278.1	6.5		1.9		bl.
[Fe VI]	5176.0	5176.2			3.3	0.11	bl. w. Fe II, Fe VII
[Fe VII]	5158.9	5158.7				0.20	bl. w. Fe II, Fe VI
[Fe VI]	5145.8	5148.2				0.19	bl. w. Fe II, Fe VII
[O III]	5006.8	5006.7	44.		26.	3.5	
[O III]	4959.0	4958.6			8.5	0.62	
H β	4861.3	4861.6			\lesssim 3.6	0.51	
[Ne IV]	4725.7	4725.4		1.8	0.88		
[Ne IV]	4714.2 - 4715.7	4714.8		0.43?	0.41		
He II	4686	4686.0		1.5	0.97	0.11	
[O III]	4363.2	4364.0	6.5	8.3	6.4	0.53	
H γ	4340.5	4341.0				0.27	
[Fe IV]	4198.2	4198.1			0.07		
?		4187.7			0.05		
[Fe V]	4180.6	4179.8			2.1		bl. w. He I 4169
[Fe V]	4071.2	4070.9	3.0		1.3	0.11	
[Fe III]?	4046.2	4045.0			0.04		ident.?
He I	4009.3	4009.0			0.10		
[Ne III]	3967.5	3964.8		3.4			bl. w. He I 3964.1
[Ne III]	3868.8	3868.1	20.	9.5	6.8 ^b		
[Fe V]+[Fe VII]	3757.6+3758.9	3757.7	6.3	3.4	9.0 ^b		bl.
[Fe VII]	3586.3	3585.3		2.1			
[Ne V]	3425.9	3419.0	15.				
[Ne III]	3342.4	3343.6		3.8			

^aObserved fluxes in units of 10^{-16} erg s⁻¹cm⁻².

^bActually measured in 11 May 1997 spectrum.

Table 3. Fluxes of intermediate lines

Line	Rest wavelength (Å)	Observed wavelength (Å)	Flux ^a				Notes
			22 June 1996	6 Feb 1997	11 April 1997	12 June 1999	
O I	7771.9-7775.3	7773.5	1.4		2.0	1.1	
[O II]	7319.9, 7330.2	7326.5	5.3		4.6	5.4	bl. w. He I, Ca II
[O I]	6300.3, 6363.8	6335.2	4.5		3.2	4.4	
[O III]	4959.0, 5006.8	5006.7	54.		39.	9.5	
Mg I]	4571.1	4574.1	1.8	1.3	1.8	1.6	(+4583)
[O III]	4363.2	4380.7		5.3	4.7	1.2	bl. w. H β
Mg I	2852.1	2862.3		2.5			bl. w. Mg II & Fe II
Si III], C III]	1882.7, 1892.0, 1906.7, 1909.6	1899.3		21.			bl.
N III]	1746.8 - 1753.4	1752.9		2.1			
O III]	1660.8, 1666.1	1658.8		9.9			
C IV	1548.9, 1550.8	1548.0		7.6			
N IV]	1483.3-1487.9	1492.5		2.2			flux uncertain
Si IV, O IV]	1393.8, 1402.8, 1397.2 - 1407.4	1406.3		6.7			bl.
Si II, O I	1304.4, 1309.3, 1302.2 - 1304.9	1310.0		2.1			ident. uncertain

^aObserved fluxes are in units of 10^{-15} erg s $^{-1}$ cm $^{-2}$.

Table 4. Fluxes of broad lines

Line	Rest wavelength (Å)	Observed wavelength (Å)	Flux ^a				Notes
			22 June 1996	6 Feb 1997	11 April 1997	12 June 1999 ^b	
He I	10830	10827.6				6.0	
Pε, He I,[S III]?	9545.7, 9529.3, 9532.0	9544.0	3.0			0.70	
Pζ	9229						
Fe II	9196.9-9218.2					0.18	bl.
Fe II+He I	9175.9, 9078.1, 9174.5	9177.5	7.0			1.0	bl.
Fe II	9122.9, 9132.4	9133.8	2.0			0.39	bl.
Fe II	9070.5, 9077.4	9071	0.54			0.07	bl.
Pη	9014					0.07	bl.
Ca II	8662.1	8668.2			0.27		bl. H I, Ca II
H I	8598.3	8601.7			0.07		bl.
H I, Ca II	8545.4+8542.1	8545.9	0.20		0.22		bl.
Ca II	8498.0	8496.9			0.80		bl.
O I + Fe II	8446.5 + 8451.0	8448.1	8.4		3.5	0.88	bl.
He I	8285.4	8287.3	0.16		0.12	0.05	
Fe II	8228.9	8227.7	0.72		0.53	0.11	
He I	8155.8	8156.3			0.02	0.02	
He I	7971.6	7970.7	0.08		0.22	0.05	
?		7892.0			0.14		narrow?
?		7610.4			0.07		narrow?
He I	7281.0	7277.7			0.46		bl. w. [O II]
Fe II	7155.1, 7172.0	7156.7			0.21		mult. 14
He I	7065.3	7063.5	2.0		1.2	0.40	
He I	6678.2	6675.6	0.60		0.33		
Hα	6562.8	6562.4	330.		160.	30.	
[O I]	6300.3, 6363.8	6335.2	4.5		3.2	4.4	
Fe II	6148, 6149	6146.3			0.19		mult. 74
He I	5875.7	5876.4	3.8		2.5	0.88	
[N II]	5754.6	5753.5	0.39		0.27	0.11	
Fe II	5534.9	5533.2			0.13		mult. 55, bl. w. [O I] 5577
Fe II	5414.1, 5425.3	5421.1			0.18		mult. 48+49
Fe II	5362.9	5367.1			0.22		mult. 48
Fe II	5316.2	5317.9			0.54		mult. 49
Fe II	5265, 5276.0	5273.9			0.10		mult. 48+49
Fe II	5169.0	5169.5	2.6		1.0		mult. 42, bl. w. [Fe VI], [Fe VII]
Fe II	4629.3	4627.6			0.25		mult. 37
Hβ	4861.3	4861.6	8.8		4.3	1.2	
He II	4685.7	4686.0	0.77	0.24	0.26		
He I	4471.5	4470.7	1.1	0.63	0.68	0.26	
[O III]	4363.2	4380.7		5.4	4.7	1.2	bl. w. Hβ
Hγ	4340.5	4341.0		4.6	3.4	1.1	bl. w. [O III]
Fe II	4233.2	4238.9			0.48		mult. 27
Fe II	4178.9	4180.3			0.22		mult. 28, bl. w. [Fe V] 4180
He I	4120.8	4122.4			?		
Hδ	4101.7	4102.3	1.7		1.6	0.78	
[Ne III], Heε	3967.5, 3970.0	3967.8	2.2		0.93	0.30	blend w. Fe V, Heε
Hζ	3889.0						
He I	3888.6		1.5				

Table 4—Continued

Line	Rest wavelength (Å)	Observed wavelength (Å)	Flux ^a				Notes
			22 June 1996	6 Feb 1997	11 April 1997	12 June 1999 ^b	
H η	3835.4		1.2	1.1			
[Ne V]	3426	3447	1.8				
?	?,	3075.4		0.58			uncert. id.
?	?,	3001.1		0.35			uncert. id.
O III	?,	2983.5		0.36			uncert. id.
Fe II, [Mg V]	2926.6, 2928.3	2925.8		0.23			mult. 60, ident. uncert.
Mg II	2795.5, 2802.7	2793.3		130.			
He I + Al II]	2663.4+2669.2	2666.3		0.71			
Fe II	2614.9-2631.0	2617.7		3.9			mult. 1+171
Fe II	2585.9 -2593.7	2592.0		0.85			mult. 1+64
Fe II	2562.5, 2563.5	2561.3		0.35			mult. 64
Fe II	2506.4-2508.3	2505.6		2.0			
Ly α	1215	1210.9		300.			

^aObserved fluxes are in units of 10^{-15} erg s⁻¹cm⁻².

^bIncludes some measurements from the 13 May 1999 VLT spectrum, especially in the near-IR.